CENTRO DE INVESTIGACIONES
EN OPTICA, A.C.

"NONLINEAR EFFECTS IN THE TERAHERTZ BAND"

Tesis que para obtener el grado de Doctor en Ciencias (Óptica)

Presenta: Jorge Ludwig Regalado de la Rosa

Director de Tesis: Dr. Enrique Castro Camus

León · Guanajuato · México
Diciembre de 2021

Vo. Bo. Dr. Enrique Castro Camus
Director **de tesis**

Abstract

Nonlinear Effects in Terahertz Band

by Jorge Ludwig Regalado de la Rosa

In this thesis I present an experimental study of the terahertz emission from $In_xGa_{1-x}As$ epitaxial layers that were grown while varying the alloy fraction x. It was observed that a terahertz emission that is significantly different depending on the variation direction (towards the surface/bulk) of the alloy fraction. We attribute the difference to the significant change of the band bending induced in the growth direction and to the position-dependent variation of the effective mass. Additionally, I present the results of an investigation of the nonlinear effects induced by different incident THz fields, leading to a field-dependent transmission enhancement in doped InGaAs. The underlying physics behind this phenomenon is inter-valley scattering induced by the electric field of the THz pulse over the pico-second time scale. We simulated three different open aperture Z-scan experiments, for 0.1, 0.5 and 1 ps THz pulses duration and a doping level of 2×10^{17} cm^{-1} varying the THz pulse amplitude propagating through the sample from 1 to 1000 kV/cm. We found an enhancement in the transmitted field as well as higher frequencies generations as the pulse's amplitude increases.

Acknowledgements

Desde mi ingreso al doctorado el 4 de septiembre de 2017 conté con el apoyo de muchas personas del CIO, quienes en mayor o menor medida contribuyeron a que concluyera exitosamente el programa. Primeramente quiero agradecer a todos mis docentes de asignatura, quienes gracias a su dedicación y paciencia me permitieron adquirí conocimiento no solo académico: Dra. Alejandrina Martínez, Dra. Gloria Vázquez, Dra. Reyna Duarte, Dr. Carlos Pérez, Dr. Roberto Martínez, pero especialmente al Dr. Geminiano Martínez Ponce por sus excelentes clases de Óptica Física las cuales a menudo recuerdo como las clases más estimulantes que tuve durante el doctorado; adicionalmente quiero agregar a este agradecimiento especial al Lic. Mario Ruíz, quien fue mi profesor de inglés y un amigo a quien acudí por consejo cuando la situación lo ameritó; sin duda con él aprendí a escribir y hablar el inglés con el que hoy escribo esta tesis. Sin embargo, en el camino hubo más personas además de los docentes, me refiero al personal del CIO que me apoyó en la construcción de piezas para los experimentos o simulaciones que realicé como Diego Torres del laboratorio de electrónica, Jesús Ortiz del taller mecánico y José Ignacio Diego de Sistemas.

Hablando del personal aceémico, quiero expresar mi agradecimiento a quienes formaron parte de mi comité de seguimiento acedémico, los doctores Roberto Ramírez, Bernardo Mendoza y especialmente a Ramón Carriles, quien además de formar parte de mi comité de seguimiento estuvo a punto de convertirse en mi director de tesis hacia el final de mi posgrado y no voy a olvidar nunca el hecho de que me haya tendido la mano cuando hubo una crisis ajena a lo académico que estuvo a punto de afectarme. Adicionalmente quiero agradecer a las personas con quienes estuve más en contacto, mis compañeras y compañeros del grupo de terahertz, Goretti Hernández, Mónica Ortiz, Eve Lambert, Abhishek Singh y Edgar Reyes con quienes compartí risas, café y cerveza en contextos sociales, académicos y en algunas ocasiones deportivos hasta donde la pandemia lo permitió. Pero qué habrá sido de mi doctorado sin el apoyo de quienes crecieron las muestras en la Universidad Autónoma de San Luis Potosí, el Dr. Víctor Méndez y el M. C. Alfredo Belio; con ellos también estoy muy agradecido por el apoyo en todas las fases del experimento.

A mi futura esposa quiero agradecerle el apoyo emocional y comprensión que tuvo para mi cuando me veía frustrado y trabajando a altas horas de la noche o en fines de semana sin tener éxito. Sé que sus consejos me los daba como parte de la experiencia que ya había tenido durante su doctorado y, aunque no siempre le hice caso, sé que tenía razón y estoy muy agradecido con ella por darme apoyo cuando más lo necesitaba.

A mi asesor, el doctor Enrique Castro Camus quiero agradecerle sus llamadas de atención, críticas, asesorías y consejos, pues gracias a eso y a pesar de que hace dos años que no colaboramos en persona, hoy estoy culminando el doctorado. Además de esto, quiero agradecer su paciencia y apoyo sobre todo en este último año que ha sido muy difícil no solo por la pandemia y la distancia que a veces nos impide colaborar de la mejor manera, si no porque en tiempos recientes surgieron situaciones complicadas para él y su familia y aún así nunca me dejó de apoyar.

Al Consejo Nacional de Ciencia y Tecnología le agradezco la beca 589852 que me otorgó para mis estudios de doctorado. En este agradecimiento van incluidos las y los contribuyentes porque gracias a sus impuestos, es que tuve la oportunidad de obtener el más alto grado académico sin pagar un solo peso de colegiatura. Les aseguro que esta inversión que CONACyT ha hecho en mi, no será en vano.

Finalmente le quiero agradecer al CIO como institución por haberme abierto sus puertas hace más de cuatro años cuando era estudiante de maestría. Ahí aprendí todo lo que hace unos meses me permitió conseguir un buen trabajo, que aunque no es en el ámbito académico, me llena de placer pues es impresionante cómo el conocimiento que adquirimos quienes estudiamos ciencia es tan útil en la industria y ni la gente de ahí ni nosotros lo sabemos.

Contents

The needs of the many outweigh the needs of the few...

Spock, Science Officer, USS Enterprise

Chapter 1

Introduction

These are great times to be a physicist. In the last twenty years many Nobel prizes have been awarded for astonishing discoveries in physics: the accelerating expansion of the Universe[1, 2], the theoretical postulation of the Higgs Bosson[3, 4], the invention of graphene[5], the theorectical discovery of topological phase transitions and topological phases of matter[6, 7], the invention of the optical tweezers[8] and a method for generation of high-intensity, ultra-short optical pulses[9] and, last but not least, the discovery of gravitational waves[10]. These are just a few of the amazing breakthroughs in physics that scientist have been able to witness, giving us the motivation to pursue a research career that, brings us closer to making a contribution to the human knowledge.

In that sense, it is worth to point out, that many great discoveries in physics have lead to significant technological advances, which made life more comfortable, enhanced human life expectancy among other benefits. Yet, many of those advances started in some laboratory, somewhere in the world, just as a publishable idea that would not have been possible to take out of the lab without industry people.

The industry has been a close friend of physics since the inter world-war period[11], when many industrial laboratories employed a considerable number of US physicists and generated not a small amount of papers published in US journals[12]. However, not many physicists approved this physics-industry friendship in the early 1900's because science, previously recruiting a few, had become a vocation for many[13]. But thanks to the collaborations between academy and industry, and the efforts of many people, gradually the way was paved for the emerging of Solid State Physics as an exciting new field of physics that, in the early Cold War, attracted many PhD students opening new positions in universities and industrial laboratories. A success of the arising of this field, was the transistor, invented in 1947 by Bell Labs physicists working with semiconductors. How would life be without the transistor or semiconductors? Surely, pretty rudimentary.

Semiconductor devices are the cornerstone of the electronics industry, which by the way is one of the biggest industries in the world[14]. These devices have been important to our lives, and now modern civilization is almost unimaginable without them. Almost all our machines use electronic controls; computers perform calculations of complexity that were previously impracticable; administration is supported by information processing machinery. Financial institutions like banks, insurance companies and government agencies rely increasingly on computers. Medium size and even small companies take advantage of the most modern electronic book-keeping and stock control systems because this promises to be more reliable and accurate than the traditional methods, reducing the human mistakes practically to none.

The amount of data and the speed with which it is communicated between humans and machines increases steadily. Modern electronic entertainment is also a way of transmitting the information. For example, lets consider a simple recreational activity involving solid state-based devices: reading a book on a cellphone. It would not be possible to read a book in a flat-3-inches-crystal-screen, embedded on a computer that weighs not more than 200 gr, and fits on a hand. Undoubtedly, science advances are so overwhelming that in our daily life, we ignore them and enjoy their features: low cost (in many cases) and easy-to-use. Nevertheless, this availability and low cost come with a cascade of issues; many people in the world have at least one device, which consumes an enormous amount of both energy and data, leading us to several technological challenges among which are energy storage and wireless data traffic.

1.1 Problem approach

Consumer demand for a range of image-rich services and mobile apps has driven a continuous increase in wireless data traffic. At the beginning of the century, Edholm's law predicted that wireless data volumes would double every 18 months[15]. However, the prediction was overridden by the latest report from Cisco's visual networking index[16]. The report showed an increase in global monthly mobile data traffic from 2.1 exabytes in 2014 to 3.7 in 2015 and did forecast exponential growth in the demand for faster mobile connections due to the increasing proportion of 4G mobile connections and the rise of 5G technology. This situation is mainly due to the appetite of users for applications such as HDTV and high-quality video-conferencing, which have been enhanced by the COVID-19 outbreak, issues that demand access to large amounts of data, and for sure, this demand will not diminish in the upcoming years.

Nowadays, the lower frequency bands of the electromagnetic spectrum fulfil the data traffic demand, but right now, the radio, television, cellular, Wi-Fi, radar, and other

uses are filling these bands out. The widely known Wi-Fi, is a license-free spectrum that comes with low implementation costs and ease of access, but it is limited to the assigned bandwidth[17]. Wi-Fi capacity based on IEEE standards can provide speeds of up to 100 Mb/s at 2.4 GHz, or 433 Mb/s in the 5 GHz frequency band[18]. Wider spectral bands have been allocated at millimeter-wave frequencies from 30 GHz to 100 GHz, with a total bandwidth of less than 7 GHz, and these bands support data rates up to 10 Gb/s. The terahertz (THz) frequency region, currently unallocated, offers the potential for systems with much larger bandwidth, ranging from a few GHz to more than 100 GHz. So, a variety of international standards organizations are exploring the technical and operational characteristics of services in the unallocated frequency range above 275 GHz[19]; and research groups around the globe, supported by both industry and government funding, are moving forward with R&D in THz wireless link technology.

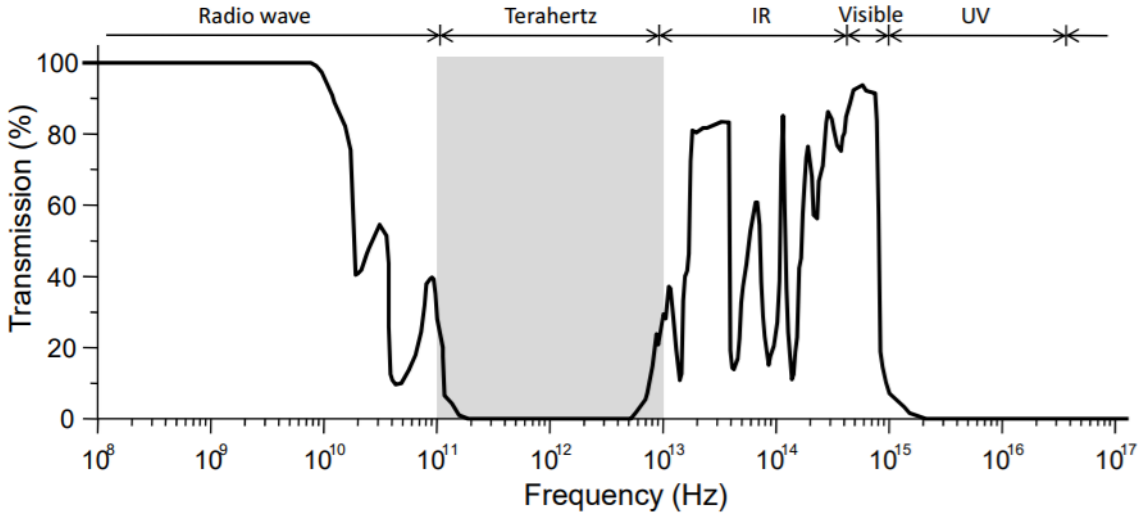

FIGURE 1.1: Atmospheric transmission spectrum of electromagnetic waves (based on figure from Lee [20])

One technical issue with terahertz technology comes from the fact that we lack of compact, efficient generation and detection systems, which has limited access to the THz communication bands. Nevertheless, the advances in device technologies could enable short-range (less than 100 m), high-capacity (greater than 10 Gbit/s) transmission in the THz region for wireless technologies. Although, another impediment for millimeter-wave and THz systems lies in free-space attenuation and molecular absorption, particularly due to water vapor as shown in figure 1.1 where it is clear that for terahertz band, the transmission in the atmosphere is highly attenuated.

1.2 Motivation

The THz band could address the upcoming problem related to data traffic because the methods for generating and detecting THz signals have advanced considerably in recent years. The main objective is to obtain a high-quality THz pulse with high-output power, which is necessary for radio communication and other THz applications. Either electronic or photonic devices can generate such signals, although the photonic approach has several advantages. To begin with, it can generate THz signals compatible with wireless over-fiber distribution to integrate them into existing, low-loss optical fiber networks. Such an approach also allows amplitude and phase modulation with high-speed data.

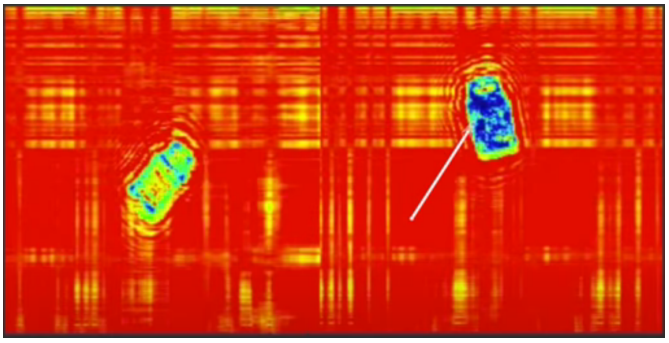

(a) Packing inspection. Left-hand jar is empty whereas the right-hand is filled with pharmaceutical pills

(b) Security inspection.

FIGURE 1.2: THz radiation application examples (Pictures from Tera Sense)

Nonetheless, despite the progress in THz photonics technology and integration, there is still a long road to be walked, and although there are a few areas with many challenges regarding THz technology, this work is focused in one particular area: wireless transmitted power. The reason is that the current THz transmitters still lack output power and are also limited by physics because THz radiation suffers high attenuation in atmosphere due to water vapor in the distances that wireless communications require.

In this sense, it is primordial to develop new high power terahertz sources and detectors. Not only because of the increasing data transmission issue, but because there are many attractive applications of terahertz radiation besides basic research, such as biomedical diagnostics [21, 22, 23, 24], security screening [25, 26, 27], material inspection [28, 29, 30], cultural heritage preservation [31, 32, 33], biological inspection [34, 35], to name just a few of the almost uncountable terahertz radiation applications.

The future exploration of nonlinear THz dynamics in materials requires an efficient and accessible table-top high power and high-intensity THz source, which demands improvements to the conventional optical rectification techniques used for spectroscopy. Recently, advances in intense table-top terahertz sources and broadband detection techniques have opened up a new phase of nonlinear terahertz research of materials to gain a deep understanding of the ultrafast nonlinear phenomena for the next generation of semiconductor-based electronic or even photonic devices.

This thesis is organized as follows:

- In chapter number two, I present an overview of the applications of terahertz radiation, as well as a description of the methods and techniques I used in this thesis.
- In the third chapter, Monte Carlo simulations of ultrafast nonlinear optical properties of doped InGaAs is discussed.
- Experimental work carried out to generate THz from gradient In_xGaAs_{1-x} surfaces is presented in the fourth chapter.
- Finally, in the last chapter, the reader can see the conclusions and perspectives.

Chapter 2

Terahertz

More than 30 years have gone by since the realization of the first coherent broadband THz sources at Bell Labs, based on the free-space photoconductive switch developed by Auston [36], Auston and Cheung [37]. Since those days, many scientific advancements have been made, including THz pulse generation, detection, time-domain and time-resolved spectroscopy, and THz imaging. This have revolutionized the THz optics field, leading to enormous advances in fundamental physics and a wide range of practical technological applications [38, 39].

THz waves have been widely used as a noncontact probe of material properties with high sensitivity [40, 41, 42, 43, 44]; in particular, to study charge carrier dynamics in semiconductors that originates from the fact that the response of charge carriers is strong and dispersive in the THz region of the electromagnetic spectrum [45]. Terahertz time-domain spectroscopy (THz-TDS) has been the most utilized ultrafast optical technique to determine the broadband complex conductivities in steady-state and transient systems, respectively [46].

Up to now, it looks like THz science and technology offers many potential technological applications for the industry, society, and scientific community. But, what is terahertz radiation? How can we detect it? Is it possible to generate it easily? In this chapter, these and a few more questions will be answered.

2.1 What is Terahertz?

Terahertz radiation is electromagnetic radiation, whose frequency lies between the microwave and infrared regions of the spectrum as shown in Fig. 2.1. A different way to understand this is to see terahertz as the radiation located between the upper limit

accessible with conventional electronic emitters and sensors, and the lower limit accessible with optical tools. Even though its lower limit is accessible with optical sources and detectors, it is impossible to see THz radiation with the naked-eye because it shares its spectrum with far-infrared radiation. This region of the electromagnetic spectrum covers from 0.1 to 10 THz (some authors claim that up to 30 THz) or, speaking in most common optical words, its wavelength spans from 3 mm to 30 microns.

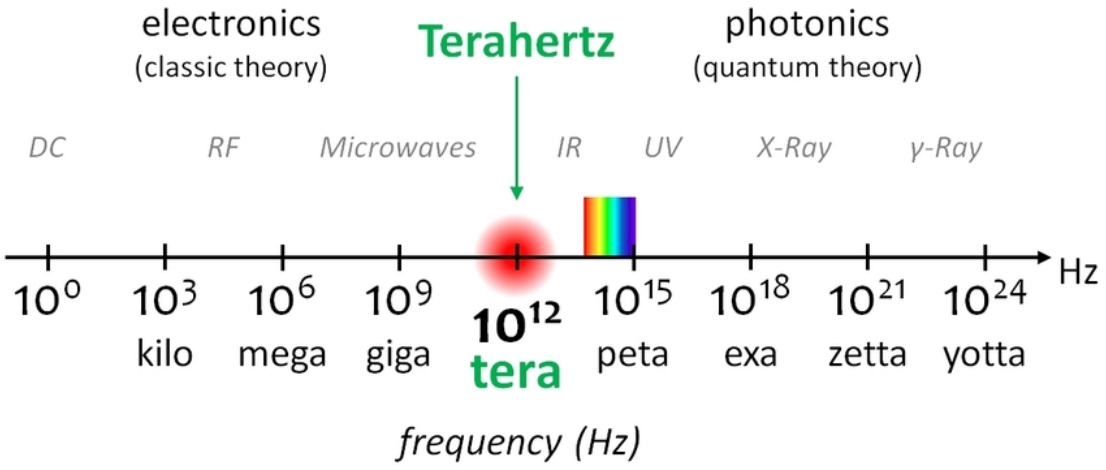

FIGURE 2.1: Terahertz band in the electromagnetic spectrum.

Although this region of the spectra looks easy to access, it remains unexplored mainly due to the technical difficulties of making efficient and compact THz sources and detectors and physical obstacles such as high water absorption. However, these technological inconveniences have been addressed by many research teams during the last four decades.

The THz region covers a wide range of fundamental excitations and resonances in molecules and solid-state materials. Hence, the broadband spectrum of a THz pulse is a convenient tool to access fundamental modes of many physical phenomena: free carrier attenuation, low energy excitations, optically active vibrational modes, and collective modes in the condensed matter such as phonons, plasmons, excitons[45, 47].

Until quite recently, THz technologies had been developed independently by researchers from several different disciplines[20], and in practice, scientific communities use various units to describe the spectrum of THz radiation. The different units employed by the different scientific disciplines are shown in table 2.1, where c, h and k_B are the speed of light in vacuum, Plank's and Boltzmann's constant respectively.

As said before, up to now, the THz band does not have a standard definition, but it is worthy to point out that some researchers commonly use definitions that span over the spectral region between 0.1 and 10 THz, even though this range exceeds the far-IR band and intrudes on the mid-IR band, where well established optical technologies exist.

TABLE 2.1: Different units used to refer to THz band.

Frequency	ν	=	1 THz	=	1000 GHz
Angular frequency	ω	=	$2\pi\nu$	=	6.28 THz
Period	τ	=	$1/\nu$	=	1 ps
Wavelength	λ	=	c/ν	=	300 μ
Wavenumber	$\bar{k}$	=	$k/2\pi$	=	33.3 cm^{-1}
Temperature	T	=	$h\nu/k_B$	=	48K
Photon energy	$h\nu$	=	$\hbar\omega$	=	4.14 meV

So far, it has been noted that terahertz radiation has interesting properties to test different material properties such as those ones mentioned in section 1.2, but the widely used technique known as Terahertz Time-Domain Spectroscopy has been barely mentioned.

2.1.1 Terahertz Time-Domain Spectroscopy

The basic idea behind a terahertz time-domain spectrometer is to compare the waveform of a reference pulse (see Fig. 2.2 a) that propagates freely through a medium with known properties (or even vacuum) with a pulse that passes through a sample (see Fig. 2.2 b). In order to analyze the data, the frequency spectra of the transmitted and reference THz signals are Fourier-transformed to convert them from time-domain to frequency-domain, which provides us the spectroscopic information of the sample under investigation (see Fig. 2.2 c). For the case of a THz-TDS imaging system, the THz focal spot is scanned across the sample to obtain a THz image of the object of interest.

Now lets describe in detail how this system works. The initial laser beam is a femtosecond near-infrared laser pulse that passes through a beam splitter that splits it into two parts: pump and probe beam. The pump beam is modulated by an optical chopper and then focused on the THz emitter, a second-order nonlinear medium; it converts the near IR to THz radiation in response to the incident laser pulse. Then, the generated THz radiation goes to a detector, an electro-optic crystal, using two off-axis parabolic mirrors. At the same time, the probe beam gates the detector, whose response is directly proportional to the amplitude of the electric field of the incoming THz pulse. Finally, by changing the time delay between the two beams through a motorized optical delay stage, it is possible to trace the THz transient temporal profile.

Electro-optic detection of THz transients is possible when the THz radiation pulse and the probe beam coincide in a co-propagating geometry inside an electro-optic crystal. As the THz pulse and probe beam co-propagate through the electro-optic crystal, it is induced a polarization modulation on the probe beam, which depends on the electric field of the THz radiation. Then, a quarter-wave plate ($\lambda/4$) analyzes the polarization

(a) Reference pulse

(b) Sample

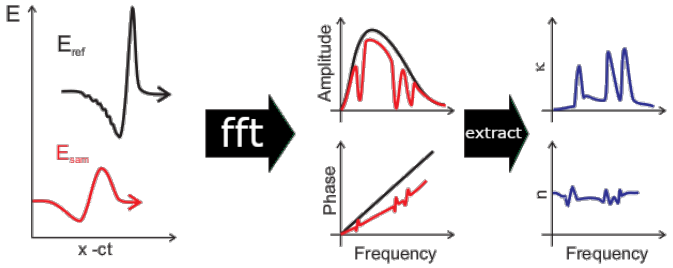

(c) Spectral analysis. Based on figure from Castro-Camus [48]

FIGURE 2.2: Basic scheme of a THz-TDS experiment.

modulation of the probe beam, and the main one is split into two beams of orthogonal polarizations by a Wollaston prism. At this point, the phase modulation of the probe beam gets converted to an intensity modulation of the two orthogonal polarizations of the probe beam, which then steers into a pair of photodiodes. Finally, a lock-in amplifier subsequently detects the difference in probe laser light intensities measured by the photodiodes.

2.2 Nonlinear Optical Techniques for Terahertz generation and detection

The linear electro-optic effect and optical rectification are nonlinear optical phenomena used to generate and detect THz radiation pulses. Generally, optical rectification refers to the generation of a DC or low-frequency polarization when an intense laser beam propagates through a nonlinear crystal. The linear electro-optic effect, also known as the Pockels effect, describes a change of polarization of a crystal due to an applied electric field. Optical rectification and the linear electro-optic effects occur only in non-centrosymmetric crystals, i. e, crystals that lack inversion symmetry and are sufficiently

transparent at THz and optical frequencies. In the following sections, a brief discussion of the most widely used THz generation and detection schemes is presented.

2.2.1 Optical rectification

Lets consider a laser electric field as

$$\tilde{E}(t) = Ee^{-i\omega t} + cc.$$

which goes upon a nonlinear crystal with second-order susceptibility different from zero and, in nonlinear optics, the crystal response to an intense laser is generally described by expressing the polarization $\tilde{P}(t)$ as a power series of the aforementioned field strength

$$\tilde{P}(t) = \epsilon_0 \left[\chi^{(1)}\tilde{E}(t) + \chi^{(2)}\tilde{E}^2(t) + \chi^{(3)}\tilde{E}^3(t) + \ldots\right]. \tag{2.1}$$

In this case, the interesting term of the equation is the one corresponding to the second-order susceptibility $\chi^{(2)}$ which is

$$\tilde{P}^{(2)}(t) = 2\epsilon_0\chi^{(2)}EE^* + (\epsilon_0\chi^{(2)}E^2e^{i2\omega t} + cc.). \tag{2.2}$$

The first term of the second-order polarization is a zero frequency term, and the second one is a contribution at frequency 2ω; so, if we consider the wave equation in nonlinear media

$$\nabla^2\tilde{E} - \frac{n^2}{c^2}\frac{\partial^2\tilde{E}}{\partial t^2} = \frac{1}{\epsilon_0 c^2}\frac{\partial^2\tilde{P}^{NL}}{\partial t^2}, \tag{2.3}$$

where n, c and P^{NL} are the refractive index, the speed of light, and the nonlinear polarization; the second term leads to the generation of electromagnetic radiation at the second-harmonic frequency, which is not relevant to the generation and detection of THz radiation by nonlinear optical techniques and therefore not discussed further. However, the first contribution in equation 2.2 does not imply the generation of radiation because its second time derivative vanishes, it leads the process known as optical rectification, a process in which a static electric field is created within the nonlinear crystal[49]. This static polarization appears in the crystal every time a fs laser pulse reaches it, generating a THz pulse whose time profile is determined by the envelope profile, typically the Gaussian-like time profile of the optical laser pulse as schematically shown in Fig. 2.3.

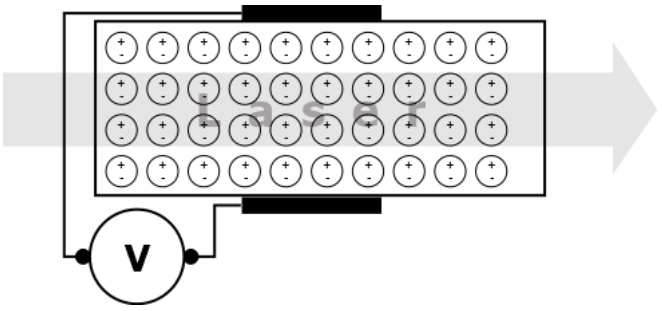

(a) Schematic representation of optical rectification

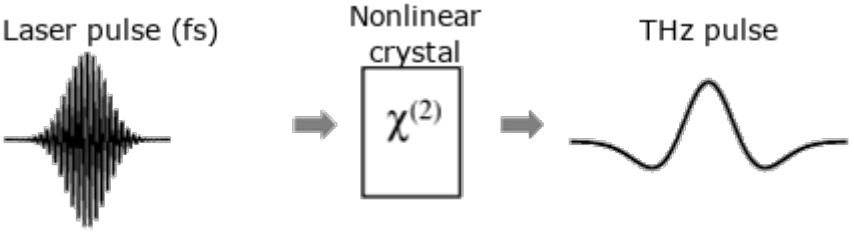

(b) Schematic generation of THz pulse through optical rectification

FIGURE 2.3: Optical rectification

2.2.2 Electro-optic sampling

The linear electro-optic effect can occur only in non-centrosymmetric materials. The effect physically means the change of the material refractive indices in linear proportion to the intensity of an applied electric field and it is related to optical rectification from the fact that the susceptibility tensor elements describing the phenomena (χ^0_{ijk}) are related to those ones describing electro-optic effect (χ^ω_{jik}) through

$$\chi^0_{ijk} + \chi^0_{ikj} = \frac{1}{2}\chi^\omega_{jik}, \tag{2.4}$$

and the relationship between the linear electro-optic coefficient r_{jki} and the linear electro-optic effect tensor element χ^ω_{jik} is given by

$$r_{jki} = -\left(\frac{4\pi}{n_0^2 n_e^2}\right)\chi^\omega_{jik} \tag{2.5}$$

where n_0 and n_e correspond to the ordinary and extraordinary refractive indices, i. e., without and with an applied electric field; and r is a third tensor known as electro-optic coefficient that depends on the material[50]. A couple examples of taking advantage of the effect are Pockel's cells, which are voltage-controlled waveplates, and also its use in the terahertz field to detect THz radiation in an scheme known as electro-optic sampling.

Electro-optic sampling can be used to detect terahertz transients. So, when an ultrashort laser pulse with a typical duration of 50fs propagates together with a terahertz transient with a width of 1ps, the laser pulse co-propagates only with a short temporal part of the transient. Hence, as they propagate, the THz transient induces birrefringence in the crystal, which becomes birrefringent, modifying the polarization of the optical pulse. Then, the quasi-instantaneous amplitude of the electric field transient becomes "encoded" in the polarization of the optical pulse, which can subsequently be separated into its two polarization components, each one sent to a separate photodetector. The difference between the readings of these two detectors is therefore proportional to the instantaneous electric field.

For this thesis, a technique involving balanced detection with two photodetectors and a lock-in amplifier was used; this technique makes possible to reach a resolution under millivolts at the photodetectors -limited by noise of course- with wave amplitudes in the electro-optical probe around 10^3kV. Hence, the technique allows to obtain a full waveform of signal by slowly varying -through a delay line- the arrival time of the probe pulse. For each delay step, the probe wave induces a change in the refractive index of the electro-optic probe, leading to a certain signal change at the photodetectors[51]. Then, after several repetitions of moving the delay stage and sampling the signal (sometimes one repetition is enough) at photodetectors after going through the electro-optic crystal, one is able to trace the waveform; and after the measurement of many waveforms they can be averaged to get rid of the noise and achieve a high sensitivity.

To sum up, the THz pulse can be traced by measuring the voltage at the photodetectors at different points of delay. To better understand this, lets observe the schematics drawn in figure 2.4-b, which shows a simple THz detection system composed of an electro-optic crystal (EOC), a quarter wave-plate (QWP), a Wollastom prism (WP), two photodetectors (PD1 and PD2), a red line representing a pulsed laser and blue-shaded triangle representing THz radiation after passing off-axis parabolic mirror. The first scheme (2.4-a) represents a THz pulse arriving at the EOC after the IR-pulse; the second one (2.4-b) THz radiation arriving at the EOC just a little bit before the IR-pulse; and finally, the last scheme (2.4-c) shows the moment when the THz pulse steers the EOC long time before the IR-Pulse. Having said that, in figure 2.4-a-i one can see the delay at 0.2mm, which corresponds to the electro-optics sampling shown in 2.4-b where the probe pulse (red solid line) arrives at the electro-optic crystal before the terahertz one (shaded blue triangle), so the voltage that photodetectors cast is equal to zero ($E = 0$). In figure 2.4-a-ii the delay is at 0.6mm, so the THz pulse arrives at the crystal before the probe (see figure 2.4-c), so that the refractive indices of the material change and the voltage coming out of detector is positive. Finally, the delay of 1mm (2.4-a-iii) leads to a negative

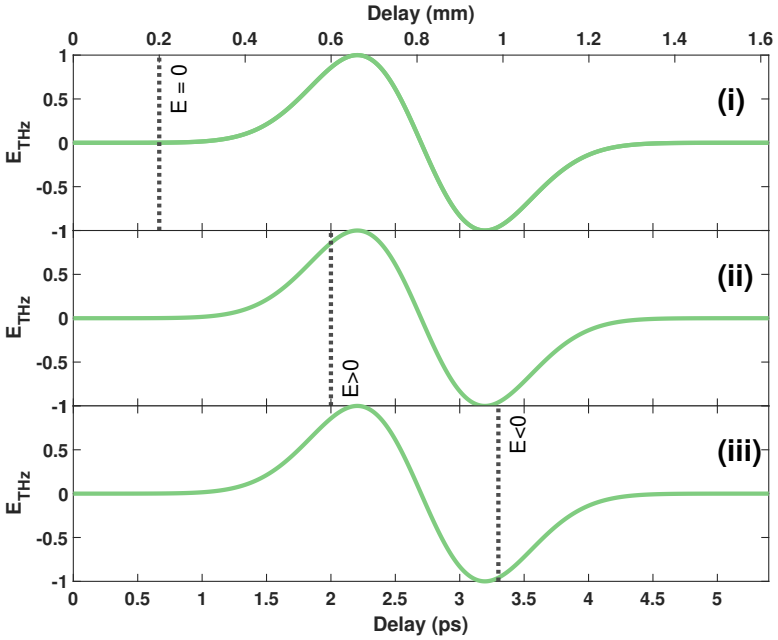

(a) Delay at $E = 0$

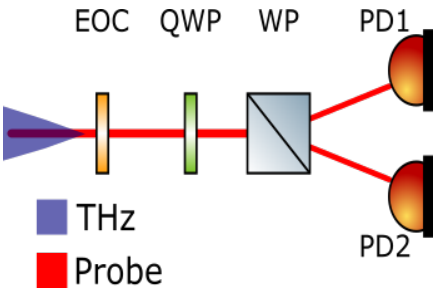

(b) Zero detector output

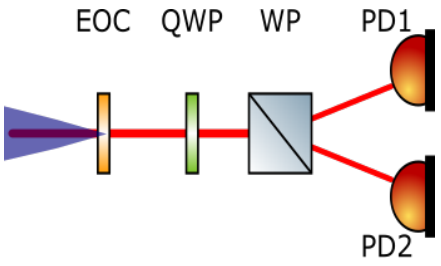

(c) Positive detector output

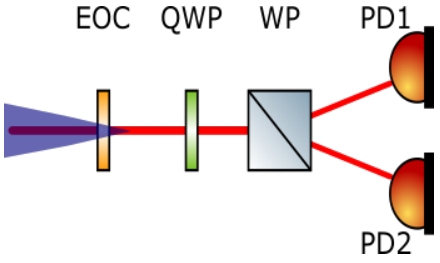

(d) Negative detector output

FIGURE 2.4: Electro-optic sampling schematics: electro-optic crystal (EOC), one quarter waveplate (QWP), one wollastom prism (WP) and two photodetectors (PD).

voltage ($E < 0$); in this case the THz pulse arrives earlier than in the previous case (see figure 2.4-d).

2.3 Other techniques for terahertz generation and detection

2.3.1 Photoconductive antennas (PCA)

Although we did not use photoconductive devices for the generation or detection of THz in this thesis, it is a widely used device used for terahertz time-domain spectroscopy, so I consider important to briefly describe how it works for completeness.

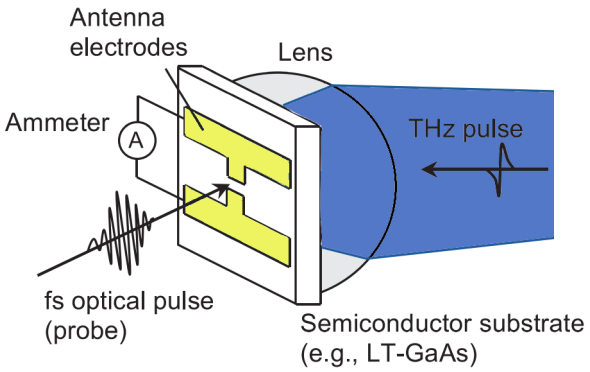

FIGURE 2.5: Schematics of a photoconductive antenna working as THz detector. Based on figure from O'Sullivan and Murphy [52].

A photoconductive antenna (PCA) is a device that exploits the increase in electrical conductivity of semiconductors and insulators when exposed to light to generate or detect radiation. The increase in the number of free carriers -either electron or holes- due to light-matter interaction leads to a change in photoconductivity easing carrier transport. Nevertheless, to abet this change the photon energy must be sufficiently large to overcome the bandgap of the material (typically GaAs for THz generation).

Regarding photoconductive detectors, the THz pulses steer to an unbiased PCA generating a time-varying voltage across the antenna electrodes. Simultaneously, the probe pulse (commonly produced by mode-locked femtosecond Ti:sapphire lasers ($\lambda = 800$ nm) incident on the gap between the PCA electrodes, excites free carriers in the semiconductor. After that, the excited carriers are accelerated by the electric field of the incident THz pulse, leading to a photocurrent that can be amplified and measured by an external circuit as shown in figure 2.5. The resulting photocurrent is proportional to the amplitude of the incoming THz radiation[52].

Chapter 3

Monte Carlo Simulations

The progress in ultrafast optics is continuously paving the way to the study of non-linear light-matter interactions in new regimes. Recent experimental observations show that the application of intense terahertz (THz) fields to semiconductors, provides new means of controlling material properties through manipulation of fundamental modes, such as free electrons and vibrational degrees of freedom [53, 54, 55, 56, 57].

With the introduction of intense single cycle pulses in the THz regime [58, 59], there have been a number of recent studies in ultrafast non-linear THz spectroscopy, which have explored ultrafast phenomena in materials upon the interaction of intense THz fields with free charge carriers, for instance: ultrafast THz induced conduction band nonparabolicity and intervalley scattering [60, 61, 62, 63], interband tunneling [64], THz-induced impact ionization [56, 65], anisotropy of effective mass within isotropic conduction bands [63],self-phase modulation [66], photoluminescent quenching dynamics [67], and femtosecond all-optical switching in nanostructures [68].

These are among the variety of interesting phenomena observed in semiconductors and semiconductor quantum dots over a time scale of pico and sub-pico seconds. However, there are more advances in ultrafast spectroscopy that open new frontiers on light-matter interactions, for example, pulses whose duration is less than a single cycle could lead to phenomena that are distinct from few-cycles ones [69].

In this chapter, we investigate how a high energy THz transient propagates through a semiconductor sample, finding that the electric field associated to the pulse increases the kinetic energy to the free carriers present in the conduction band generating intra-band scattering to side valley states. At this time, this produces an increase of their average effective mass, which leads to a nonlinear dynamic THz conductivity change that results in the reshaping of the incident THz pulse itself.

3.1 Monte Carlo simulations of ultrafast nonlinear optical properties at terahertz frequencies in n-doped InGaAs

Through the simulation of a Z-scan experiment[70] considering twelve logarithmically spaced electric-field amplitudes: 1 kV/cm, 1.87 kV/cm, 3.51 kV/cm, 6.58 kV/cm, 12.33 kV/cm, 23.10 kV/cm, 43.29 kV/cm, 81.11 kV/cm, 151.99 kV/cm, 284.80 kV/cm, 533.67 kV/cm and 1000 kV/cm, we investigated how a high energy THz transient propagates through an n-doped semiconductor sample, finding that the electric field associated to the pulse increases the kinetic energy of the free carriers present in the conduction band generating intra-band scattering to side valley states.

3.1.1 Monte Carlo Code

Our study is based on a semi-classical Monte Carlo simulation of carrier dynamics in semiconductors [71] that was initially designed for modelling the THz emission from semiconductor surfaces. This model assumes a band structure that includes parabolic Γ, L and X valleys which creates a good approximation to the realistic distribution of carrier energies[72]. In this model, a THz pulse propagating through the sample is simulated centred at $t = 0$; the semiconductor carriers move classically in 1 fs time-steps in a three-dimensional box ($6\mu m \times 6\mu m \times 3\mu m$). At every time step, the program computes the scattering probabilities considering different mechanisms: carrier-carrier, LO-phonon inter-valley ($\Gamma \rightleftharpoons L \rightleftharpoons X$), acoustic phonon, neutral and ionized impurities. After that, it uses quasi-random numbers to determine whether a particle will be scattered, its energy change and scattering angle. Then, the charge density is calculated on a fine grid of the three-dimensional box ($32 \times 32 \times 16$ divisions). From the carrier density, the Poisson equation is numerically solved in order to obtain the electric potential and from it the electric field produced by the charge distribution. At its time, this electric field, superimposed to the electric field of the incoming pulse is used to calculate the force acting on every particle in the next time step. This Monte Carlo approach provides a very detailed representation of the actual carrier dynamics in the semiconductor [73].

3.1.2 Simulation details

We performed simulations of nonlinear THz single-cycle pulses on an n-doped $In_{0.53}Ga_{0.47}As$ film with a doping concentration of $2{\times}10^{17}\,cm^{-3}$, for three different incident pulse durations: 0.1 ps, 0.5 ps and 1 ps.

The simulation starts at time $t_0 = -2.7\,\text{ps}$, to allow the extrinsic carriers to reach equilibrium before the arrival of the THz pulse, which is centered at time $t_1 = 0\,\text{ps}$. Once the pulse has propagated through the sample, the simulation keeps running for 2.7 more pico-seconds to track the behaviour of the different scattering processes, the carrier's motion and their state within the conduction band.

3.1.3 Propagation of light in conducting media

The difference between light propagation in isotropic dielectrics and conducting media, is that when speaking of conducting media, one is interested in the conduction term in the general wave equation, not in the polarization one [74]. Besides that, it is not possible to use $\mathbf{J} = \sigma\mathbf{E}$ for the current density due to the inertia of conduction electrons where σ is the DC conductivity. Hence, a treatment in which the motion of electrons under the action of a time-varying electric field becomes necessary. Such treatment is widely discussed in Fowles [74, pp. 160-163]. Having said that, the general wave equation reduces to

$$\nabla^2\mathbf{E} = \frac{1}{c^2}\frac{\partial^2\mathbf{E}}{\partial t^2} + \frac{\mu_0\sigma}{1 - i\omega\tau}\frac{\partial\mathbf{E}}{\partial t}, \tag{3.1}$$

whose solution is an homogeneous simple plane-wave of the form

$$\mathbf{E} = \mathbf{E_0}e^{i(\mathfrak{K}z - \omega t)}, \tag{3.2}$$

where ω is the angular frequency, c is the speed of light in vacuum, t is the time, μ_0 is the magnetic permeability of vacuum, τ is the scattering time, which we can obtain from the simulation and $\mathfrak{K}$ accounts for the properties of the material that in our case are expected to change dynamically; this wavevector is assumed to be complex and satisfies the relation

$$\mathfrak{K} = \frac{\omega^2}{c^2} + \frac{i\omega\mu_0\sigma}{1 - i\omega\tau}. \tag{3.3}$$

Besides that, the static conductivity is given by

$$\sigma_0(t) = e\left(n_\Gamma(t)\mu_\Gamma + n_L(t)\mu_L\right), \tag{3.4}$$

where $n_{\Gamma/L}(t)$ is the density and $\mu_{\Gamma/L}$ is the mobility in the electron in the Γ/L valley. Here we don't include the information regarding X-valley because the required energy to jump into that valley is higher than the available in the simulation. Therefore no electron jumps to X-valley. Notice that this representation, now depends both on the frequency and time the terahertz pulse that we simulated has the form $E_{THz}(t) \propto te^{-t^2/\gamma^2}$. To have also a representation that depends both on the time and frequency we can calculate the Fourier transform of the pulse, which results in an amplitude $\tilde{E}_0(\omega)$ and phase $\phi(\omega)$

spectrum. From this spectrum the original pulse can be represented as

$$E(t,z) = \int \tilde{E}_0(\omega) e^{i(\Re(\omega,t)z - \omega_l t + \phi(\omega))} \mathrm{d}\omega. \tag{3.5}$$

This expression gives the electric field for a propagation distance of z.

3.1.4 Results

Figure 3.1 shows the rates that involve scattering between the Γ and L valleys, events involving X valley (not shown) are three orders of magnitude lower. From the plots it can be seen that the number of scattering events, at their peak value, are approximately a factor of two higher for the simulation with 0.1 ps incident pulse duration than that of the 0.5 ps, and the peak rates for the 1 ps pulse are another factor of approximately two lower. Yet, although the peak value of the rates decreases as the pulse duration increases, the width of the scattering peak increases, which means that intervalley transitions occur for a longer period for pulses with longer duration.

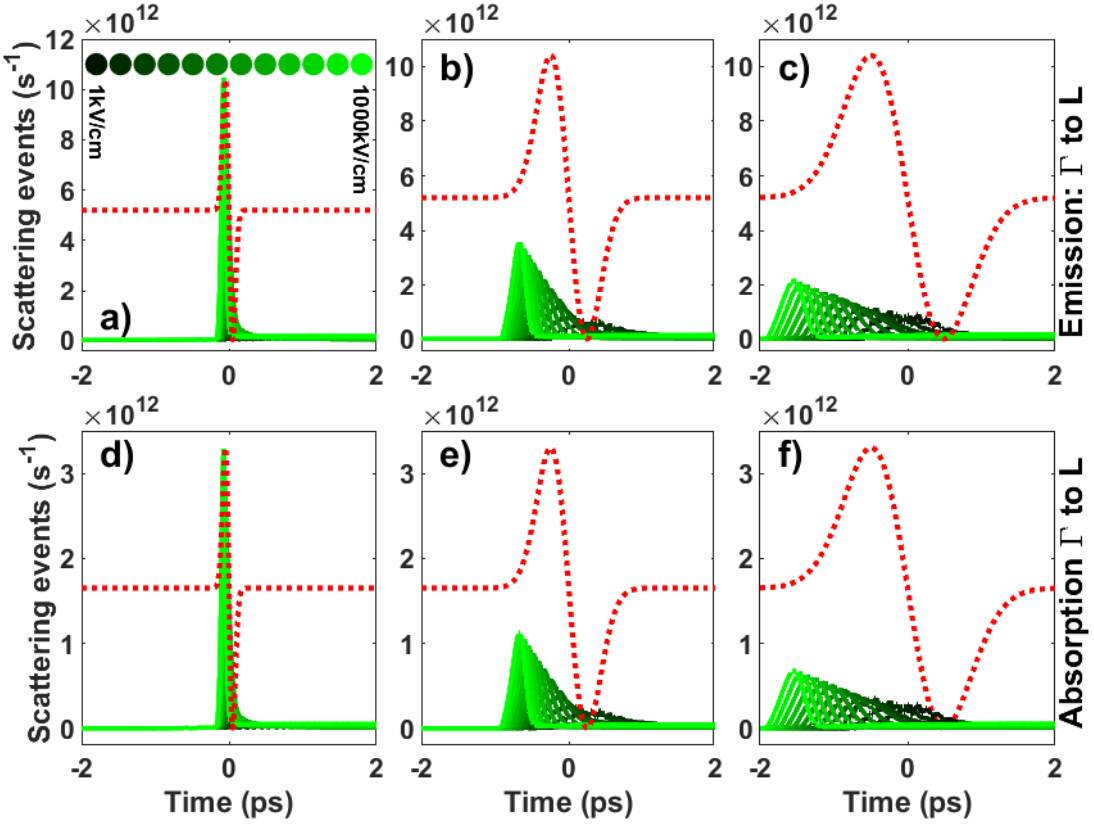

FIGURE 3.1: Optical-phonon scattering events as a function of time for different valley and THz pulse duration. a) phonon emission Γ → L, 0.1ps; b) phonon emission Γ → L, 0.5ps; c) phonon emission Γ → L, 1ps; d) phonon absorption Γ → L, 0.1ps; e) phonon absorption Γ → L, 0.5ps; f) phonon absorption Γ → L, 1ps.

Figure 3.2, shows the populations of the Γ and L valleys in the upper and lower panels respectively for the different THz pulse durations, as a visual reference the corresponding terahertz pulses are also shown (red dotted line). It is observed that the changes of the populations of the valleys are strongly related to both the pulse duration and its amplitude. The large amplitudes tend to rapidly transfer carriers to L, while less intense pulses produce slower changes of the valley populations. It is also possible to observe, that pulses with longer durations also have a more pronounced effect on the population of the valleys.

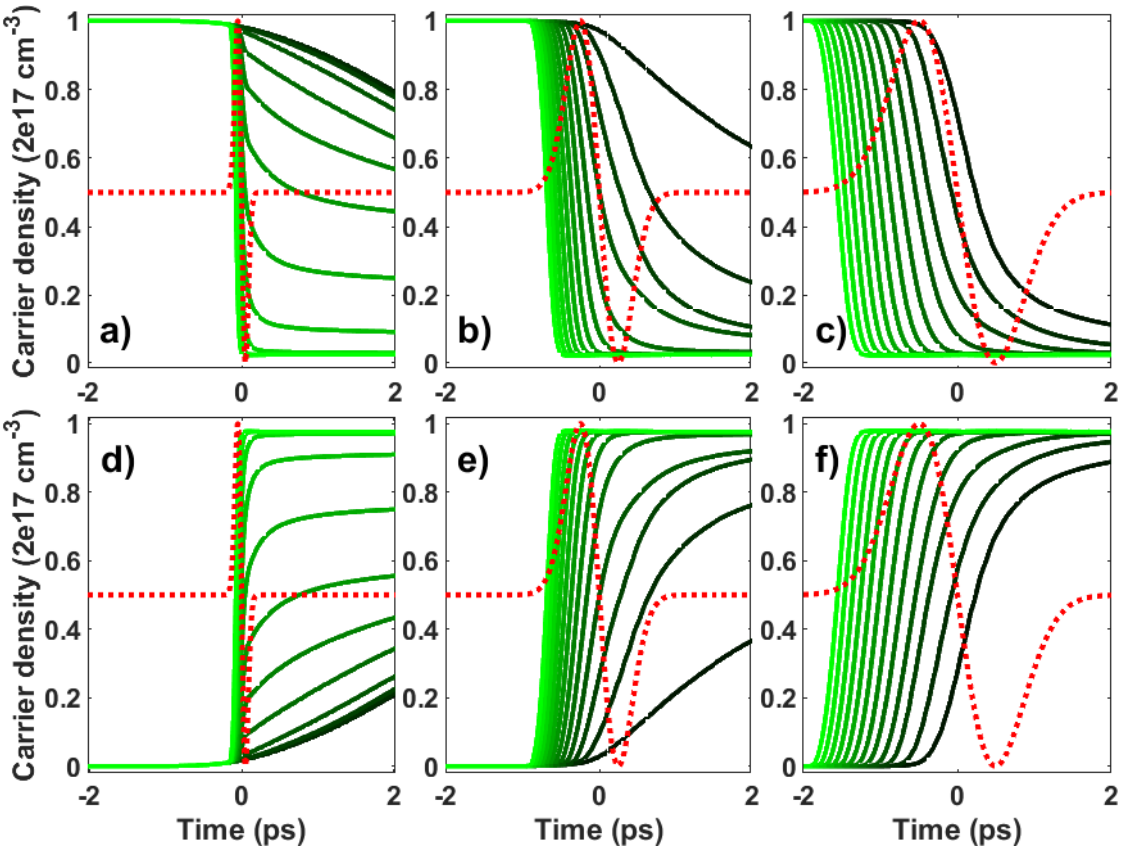

FIGURE 3.2: Valley population as a function of time for different valley and THz pulse durations: a) Γ, 0.1ps; b) Γ, 0.5ps; c) Γ, 1ps; d) L, 0.1ps; e) L, 0.5ps; f) L, 1ps. Note that the incident THz pulse duration (red doted line) drives the time at which the carriers start jumping from Γ to L valley.

Figure 3.3 (a) shows the evolution of static conductivity given by the equation 3.4 for every simulation of terahertz pulse width equal to 0.5 ps. As expected, it shows a reduction in conductivity as a function of time, due to carriers jumping from the Γ to the L valley, making the semiconductor less conductive and more transparent to terahertz radiation. The transparency change generated by the static conductivity variation, is also frequency dependent. When a terahertz pulse containing certain number of frequencies, propagates through onto a semiconductor sample, its carriers will behave differently depending on the frequencies that compose the incoming pulse as shown in the figure

3.3 (b) which displays the imaginary part of the equation 3.3; it can be noticed that, the higher the amplitude of the incident THz pulse, the absorption coefficient decreases earlier in time. In addition, from the colormaps, one can see that Γ to L valley transfer has a stronger effect on the higher frequencies; this is particularly noticeable in the intermediate electric field region. Hence, we expect the transmission of the terahertz wave to be uneven across its spectral components.

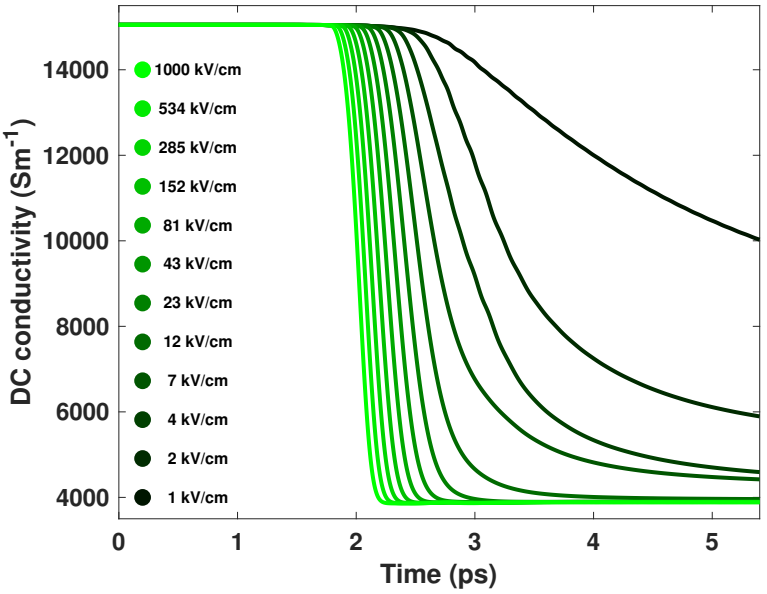

(a) Static conductivity

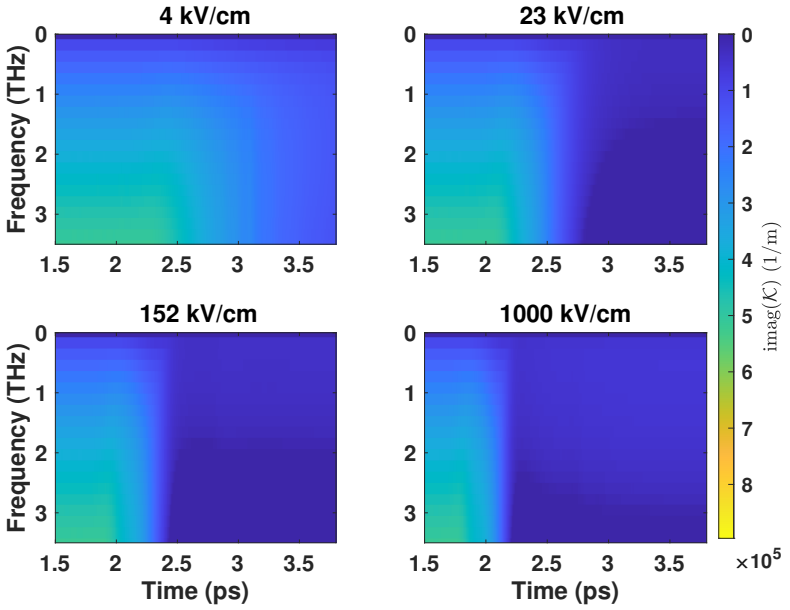

(b) Dynamic absorption coefficient

FIGURE 3.3: a) Static conductivity as a function of time for the twelve simulations of incident terahertz pulse width of 0.5 ps; b) Dynamic absorption coefficient for three simulations from 0.5 ps pulse width set.

Figure 3.4a-c shows the THz pulses after transmission through the sample for the three pulse durations, the incident pulse shape (red dotted line) is presented as a visual reference of the incident pulse. As expected, the transmitted amplitude increases with the incident one. In order to compare the effect of the amplitude on the waveform, panels a.1-c.1 of figure 3.4 show a normalized (when possible) view of three transmitted pulses for different incident amplitudes: 1.8 kV/cm, 6.6 kV/cm and 1000 kV/cm. Here it can be seen that for 0.1 ps pulse duration, the transmitted amplitude is small enough that normalization was not possible, except for 1000 kV/cm. In that case the transmitted amplitude is non-zero, yet the pulse is highly asymmetric showing only a negative peak. On the other hand, b.1 and c.1 show non-zero waveforms for all the incident amplitudes. These cases show shapes bipolar, with one positive and one negative peak, or even more than one cycle such as the 1000 kV/cm in c.1. This indicates that, as expected, the process is non-linear and frequency dependent.

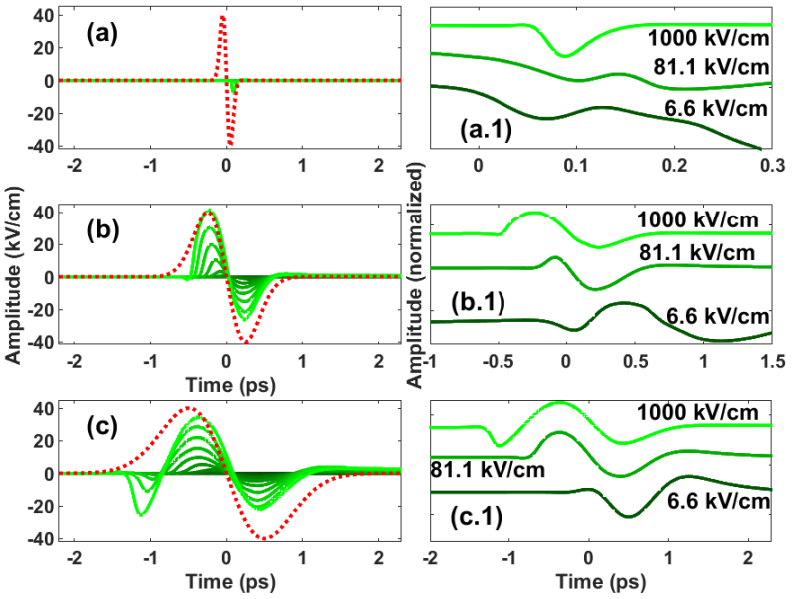

FIGURE 3.4: Transmitted THz pulses for different durations a) 0.1ps; b) 0.5ps; c) 1ps, the red dotted line depicts the incident THz pulse shape. In the right-side panels, a zoom of three transmitted THz pulses is displayed for 6.6, 81.1 and 1000 kV/cm for each pulse width.

In order to better understand the non-linear interaction between the radiation and the material, the transmitted electric field as function of the incident THz amplitude are shown in Figure 3.5 for 0.5, 1.0, 1.5 and 2.0 THz, considering a sample thickness of 500 nm. From this plot, it is possible to see that the transmitted electric field amplitude does not increase linearly as a function of the incoming amplitude; on the contrary, there is a threshold value around 23 kV/cm after which the transmission increases, more slowly than before for the pulses of 0.5 and 1.0 ps width. On the other hand, for 1.5

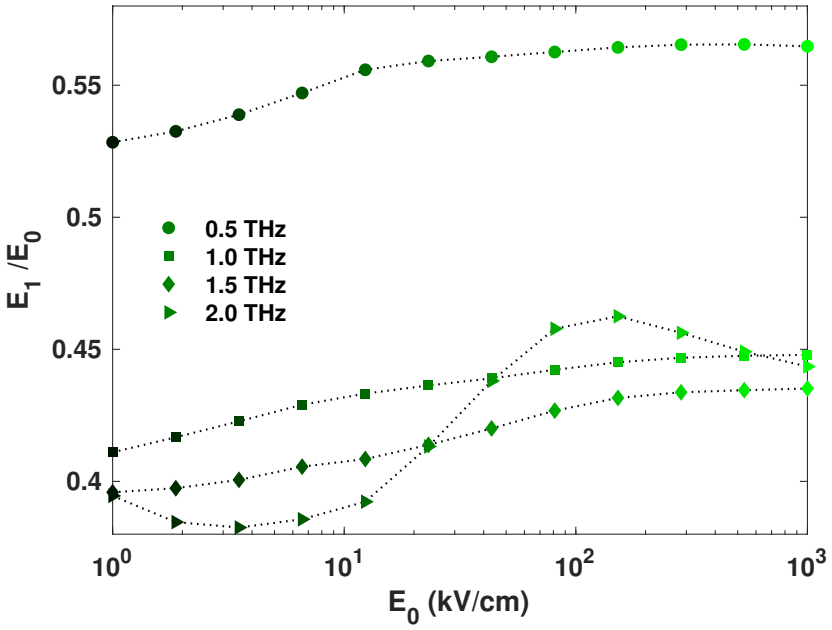

FIGURE 3.5: Transmitted to incident amplitude ratio at 0.5, 1.0, 1.5 and 2.0 THz for 0.5 ps incident pulse passing through 500 nm of material.

and 2.0 THz, it seems that the transmission through the sample exhibits an oscillatory behaviour; this is more evident at 2.0 THz, where the transmitted THz diminishes from 1 to 7 and from 81 to 1000 kV/cm while it goes up from 12 to 43 kV/cm. So, it is clear that the material presents a non-linear behaviour when different amplitude THz pulses pass through it, and is closely related to dynamic change of absorption coefficient shown in 3.3 (b).

3.1.5 Discussion and conclusions

The non-linear transmission of high-field terahertz pulses in doped InGaAs that has been reported in the literature was modeled using a Monte Carlo simulation. This formalism allows us to follow in detail the evolution of the inter-valley scatting rates, which show their peak in the vicinity of the terahertz pulse. In addition, it was possible to carefully follow the population of the valleys, showing that for pulses with low field amplitudes the populations only change slowly and the majority of the carriers remain in the Γ-valley, while large amplitudes produce fast transfer to the *L*-valley of a significant fraction of the electrons. This dynamic changes produce changes both in the waveforms and their spectra which is both amplitude and duration dependent. From analyzing the amplitude of the transmitted pulses it is possible to see that there is a threshold field, which is different for each pulse duration, where the transmitted amplitude shows a "sudden" change of magnitude. The different thresholds can be explained, at least qualitatively, in

relatively simple terms. The longer pulses accelerate carriers for longer periods, allowing them to gain enough kinetic energy to scatter to the L-valley with even lower electric field amplitudes.

In conclusion, the Monte Carlo approach presented here, allowed us analyzing in great detail the evolution of the scattering rates and valley populations during the interaction of a terahertz transient with InGaAs. Furthermore, from the conductivity obtained it was possible to calculate the transmittance of the terahertz pulses.

Chapter 4

Development of terahertz sources

Plenty of research groups worldwide have reported that InAs, InGaAs, and GaAs heterostructures are excellent materials for optoelectronic devices. The particular importance of these material alloys arises from the growing interest in THz technology, where a wide variety of devices like THz sensors[75, 76], emitters[77, 78], transistors[79] and photo-mixers[80] have been developed and yet great research efforts are still under process to reach improved characteristics. However, the growth of InAs/GaAs and InGaAs/GaAs implies a challenge due to the lattice mismatch between these materials. The mismatch promotes strain accumulation and, once it is relieved, rough epilayers surfaces with a high density of misfit dislocation get generated. Different ways of solving this problem have arisen, among which the growth of metamorphic layers have been proposed. A metamorphic structure consists of continuous varying number of layers with different indium concentrations[81] located between the substrate and the film whose crystal quality is trying to be enhanced. The metamorphic structure reduces the strain and(or) the propagation of dislocations toward the upper layers[82]. It has been reported that $In_{1-x}Ga_xAs$ graded layers can be elastically strained but are free of dislocations for a wide-spread range of indium composition[83, 84]. It is possible to construct a metamorphic structure by a compositional Indium-graded layer. There, the constitution of the alloy is intentionally changed[85, 86], propitiating band-bending as the film growth increases. As a result, under optical excitation, the initial energy of the carriers and the ballistic transport can also be favoured, which improves the main emission mechanisms for THz[87].

The work discussed in this chapter, was carried out jointly with collaborators from Universidad Autónoma de San Luis Potosí. The work consists in the development and characterization of a gradient heterostructure for terahertz generation. The growth of the sample was performed at UASLP, whereas the terahertz emission characterization

was carried out at *Centro de Investigaciones en Óptica A. C.*, where we set the experimental set-up shown in figure 4.1 to be able to produce terahertz radiation in a reflection configuration.

4.1 Terahertz generation from gradient InGaAs surfaces

The emission of terahertz electromagnetic transients from semiconductor surfaces after ultrafast photoexcitation is a topic that has attracted enormous attention over the last couple of decades[88, 89, 90, 91, 92, 93]. Not only because it provides a convenient and passive source of terahertz radiation[94, 95] but also because it is a potential tool to understand the carrier dynamics of the semiconductor material in the picosecond timescale[96].

4.1.1 Introduction

The generation of terahertz radiation at the surface of a semiconductor after photoexcitation has been attributed to two main effects. Firstly, the ballistic transport of electrons that acquire most of the kinetic energy resulting from the difference between the photon and the bangap[87]. Secondly the acceleration experienced by the electrons owing to the electric field caused by the band bending in the vicinity of the surface[97, 98]. The relative weight of these two effects strongly depends on the wavelength of the laser pulse, the bandgap of the semiconductor and the effective mass of the carriers in the material[87].

Here, it is presented a study of the terahertz emission from gradient $In_xGa_{1-x}As$ structures that was published at Phys. Lett. 119, 171111 (2021). In other words, samples in which the alloy fraction x was varied monotonously during the growth process. The resulting bandgap variation in the direction of growth brings an additional electric field in-built in the sample, which can point either towards the surface or towards the bulk. This modifies the carrier dynamics, and therefore the terahertz emission of the samples.

4.1.2 Methodology

When excited by 800 nm pulses it is well known that the THz emission of GaAs is mostly due to the carrier acceleration caused by the band-bending near the surface[97, 98] which is schematically represented in Fig. 4.2. On the other hand, for InAs, the main contribution comes from ballistic transport, owing to its very low carrier effective mass, and the rather large excess of energy of the photoexcited carriers associated to its narrow bandgap, also schematically represented in Fig. 4.2b[87]. Here, we propose two gradient

$In_xGa_{1-x}As$ structures in which the alloy fraction is continuously varied in the direction normal to the surface from 1 to 0 (Fig. 4.2c) and *vice versa* (Fig. 4.2d).

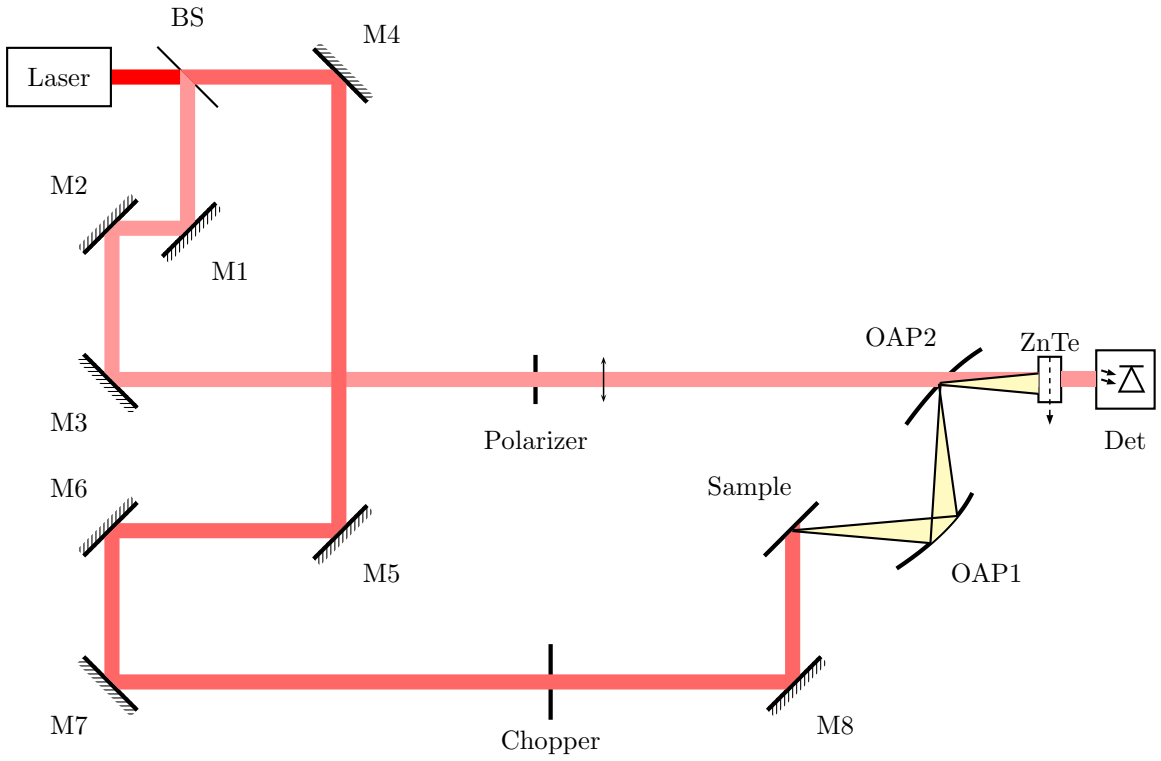

FIGURE 4.1: Free-space terahertz time-domain spectrometer in reflection configuration. Mirrors 6 and 7 move along the beam direction (delay line).

The following samples were grown by molecular beam epitaxy. The substrate temperature was set at 525 and 605° C for the growth of InAs and GaAs, respectively, and it was linearly changed between these values for the growth of the gradient structures. All samples were grown on SI-GaAs (100) substrates.

1. **GaAs**: A 1 μm thick GaAs layer with an estimated carrier density of $1 \times 10^{14}\,\mathrm{cm}^{-3}$.
2. **InAs**: A 1.5 μm thick InAs layer with a carrier density of $8 \times 10^{16}\,\mathrm{cm}^{-3}$.
3. **In>Ga**: A 0.8 μm-thick gradient layer which started with an alloy fraction of $x = 0.97$ (∼InAs) and ended with an alloy fraction of $x = 0.12$ (∼GaAs) with a carrier density of $7 \times 10^{16}\,\mathrm{cm}^{-3}$.
4. **Ga>In**: A 0.8 μm layer which started with an alloy fraction of $x = 0.12$ (∼GaAs) and ended with an alloy fraction of $x = 0.97$ (∼InAs) with an estimate intrinsic carrier density of $8 \times 10^{16}\,\mathrm{cm}^{-3}$.

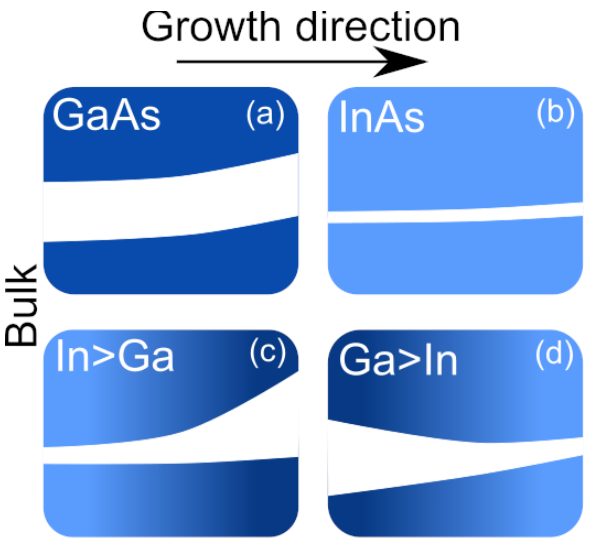

FIGURE 4.2: Schematic representations of the bandgap dependence as function of the position in the growth direction for (a) GaAs, (b) InAs, (c) InGaAs with variation from Indium to Gallium, and (d) InGaAs with variation from GaAs to InAs.

Each sample was cleaved into two pieces, one set was preserved *as-grown* and the other set was annealed by ramping the temperature slowly until reaching 250°C where an As rich atmosphere was introduced, in order to avoid surface damage, the temperature was further increased until reaching 600°C and maintained for 10 minutes[99].

All samples were studied by x-ray diffraction[100, 101]. The GaAs and InAs samples show diffraction patterns typical of the lattice constant of those two crystals and we will not discuss them here. The diffraction intensity for the gradient samples as a function of the angle is shown in Fig. 4.3a and b. What we observe is a strong peak at ∼33.03°, which corresponds to the GaAs lattice. In addition, a less prominent, but still large peak is observed at ∼30.53°, this corresponds to the 98% In lattice constant. However, these two peaks are continuously joined by a plateau of lower intensity, this demonstrates the presence of continuously varying lattice constant, consistent with the presence of a gradient. These features have been observed before in similar samples[100]. The gradient reported here is rather large, going from x∼0 to x∼1, therefore plastic relaxation of the film at certain thickness must have occurred, which lead to the low and continuous diffraction intensity plateau that corresponds to the graded film region. Additional subtle features can be seen in the curves of Fig. 4.3a and b; The small, but visible peak at around 32.6° in Fig. 4.3b for the Ga>In sample corresponds to the diffraction of a 16% indium concentration alloy, which is consistent within our error to the composition of 12% at which the gradient started. Similarly, In>Ga sample started with an In concentration of 98% explaining the peak located at 30.74° in Fig 4.3a. The slight differences with the nominal concentration for both of the gradients are related to strain. The annealing process seems to have two important effects on the samples. The plateau appears

higher for both samples, which suggests an improvement of the crystallinity along both gradients, most likely owing to the removal of lattice defects. In addition, as seen in Fig. 4.3d, the plateau of Ga>In seems to be more constant, suggesting a "softening" of the lattice discontinuity in the vicinity of the pure GaAs substrate.

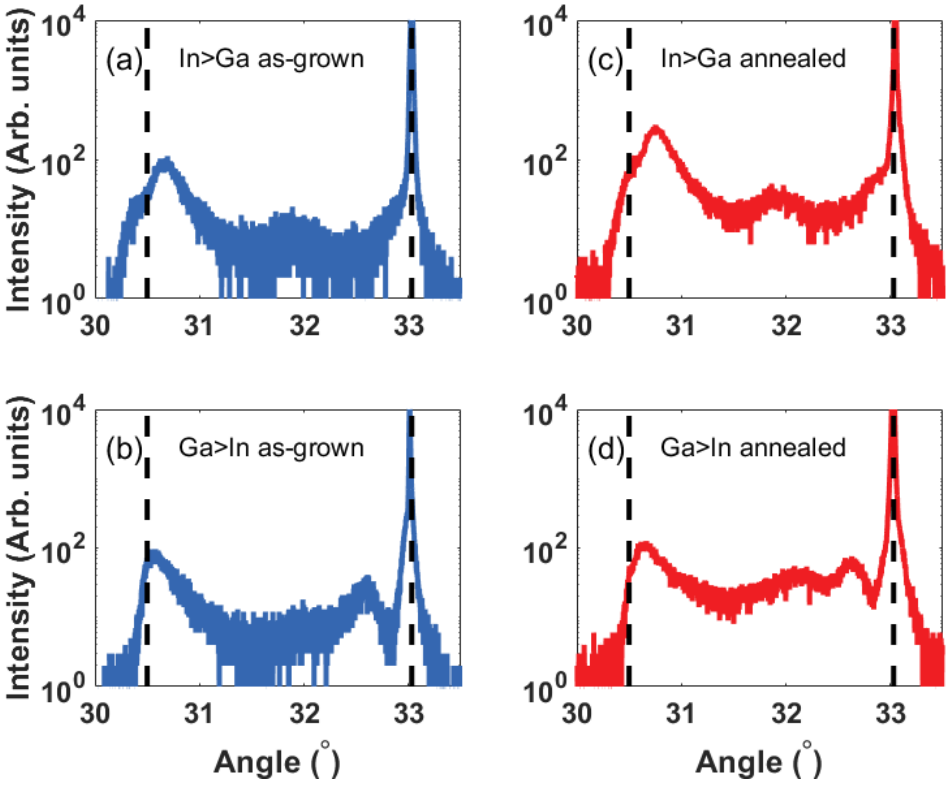

FIGURE 4.3: X-ray diffraction intensity as function of the angle for *as-grown* (a) In>Ga and (b) Ga>In samples. Panels (c) and (d) are the corresponding ones for the annealed samples.

In order to characterize the samples, a terahertz time-domain spectroscopy setup was build based on a Libra-Series Ti:sapphire mode-locked laser from Coherent® that emits pulses of ∼33 fs duration centered at 800 nm at a repetition rate of 80 MHz. The pulses are split into two beams. The first one, with an average power of ∼50 mW is sent through a motorized delay line and then is used to excite the semiconductor sample at an incidence angle of 45°. The THz radiation generated in the form of a single-cycle electromagnetic transient, is collected at 45° as shown in Fig. 4.1 by using an off axis parabolic mirror. A second parabolic mirror focuses the THz radiation onto a 1 mm thick [110] ZnTe crystal. The second laser beam is also focused onto the ZnTe crystal and copropagates with the THz radiation, subsequently an achromatic $\lambda/4$ waveplate, a Wollaston prism and a pair of balanced photodiodes are used to detect small changes in the relative intensity of the laser polarization components, which is proportional to the instantaneous THz electric field. By changing the relative delay between the THz radiation and the second laser

pulse it is possible to map-out the time-dependent waveform of the THz electric field. Further details about electrooptic sampling of THz pulses can be found in Section2.2.2.

4.1.3 Results

The time-domain signals for the four materials are shown in Fig. 4.4a and b for the *as-grown* and annealed samples respectively. Among the *as-grown* samples, InAs has the strongest emission, the second strongest signal is the one produced by the annealed In>Ga gradient sample. We calculated the integrated power of the samples, which is shown in Fig. 4.4c. Here we can see that the emission of InAs is about 13 times the power emitted by *as-grown* GaAs, while the power emitted by annealed In>Ga is about 10 times that of *as-grown* GaAs. Among the interesting things to point out in this plot is the significant reduction of the InAs power after annealing. It is also remarkable that except for the two strongly emitting materials already mentioned, the rest all have relatively similar emission powers. An exception is the annealed Ga>In sample, which shows the lowest emission of all.

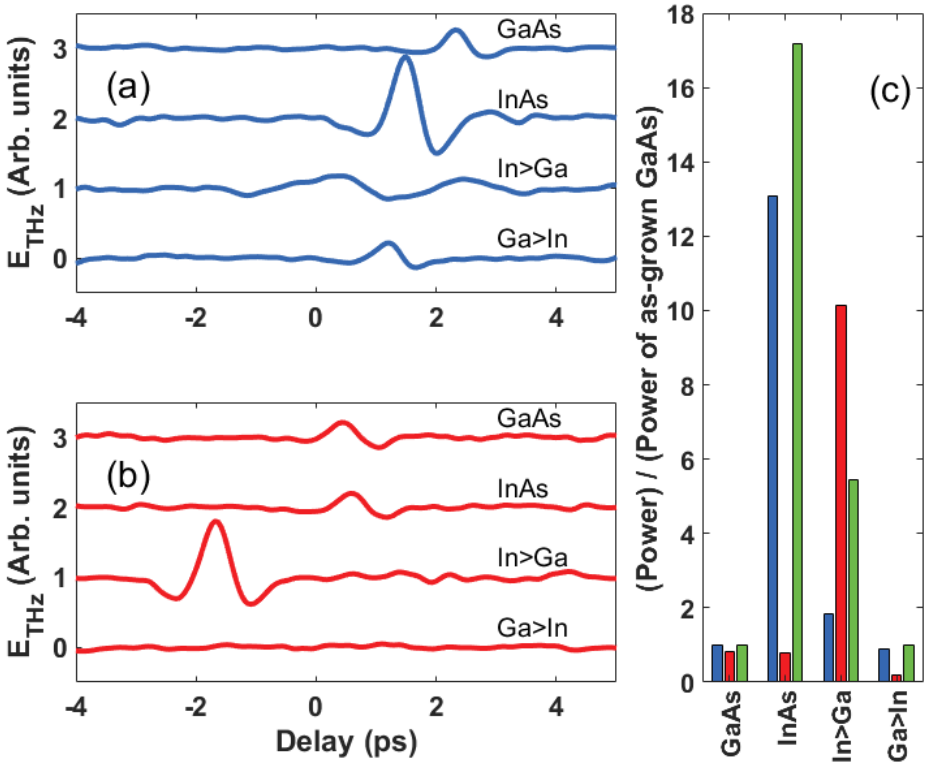

FIGURE 4.4: (a) Terahertz waveforms emitted by the *as-grown* semiconductors. (b) Terahertz waveforms emitted by the annealed semiconductors. (c) Integrated power of each emission (blue=*as-grown*, red=annealed, green=model) divided by the integrated power emitted by *as-grown* GaAs.

The annealed In>Ga sample, is a very strong emitter, almost comparable to InAs. In order to explain this, we will refer to the schematics in Fig. 4.2a-d. The In>Ga sample is composed of GaAs on the surface, which has a relatively broad-bandgap and, owing to the alloy-variation, the bandgap narrows down as we move into the bulk, this produces a strong acceleration of the electrons which adds to the acceleration caused by the surface field. In other words, the force experienced by an electron is mostly given by the difference of potential energy between the initial position, near the surface, and the final position, away from the surface. Thus, the large band bending of the gradient contributes with a significant acceleration. Furthermore, the force acting on the carrier is given by

$$F = \frac{dp}{dt} = m^* a + v\frac{dm^*}{dt}, \tag{4.1}$$

where p is the momentum, m^* is the effective mass and a is the acceleration. Therefore, the acceleration will also have an additional term given by $-v\,dm^*/dt$, in the case of the In>Ga, the derivative of the mass is negative, resulting in an additional positive term that contributes to the acceleration. In order to do an "order-of-magnitude" estimation of the terahertz emission caused by the acceleration experienced by the electrons in all four semiconductor samples (the contribution of the holes is neglected here), we assumed that the average electron was accelerated from 0 to $\bar{v_i} = \sqrt{2K/\bar{m}}$, on average, over a period δt ~100 fs which is about 2 to 3 times the duration of the laser pulse, where K is the kinetic energy, given by the difference between energy of the λ=800 nm photons and the bandgap energy at the surface $K = hc/\lambda - E_{BG}(0)$. In addition, if we make the right-hand-side part of Eq. 4.1 equal to $-\mathrm{d}U/\mathrm{d}x$ the gradient of the potential, which we can approximate as a linear function that changes $\sim E_{BG}(0)/2$ about half the bandgap energy at the surface for all samples owing to surface pinning, plus the bandgap change owing to the alloy variation for the In>Ga and Ga>In samples. Therefore in total the acceleration experienced by the electrons will be approximately

$$a = \frac{\bar{v_i}}{\delta t} - \frac{1}{\bar{m}}\left(\frac{1}{2}\frac{E_{BG}(0)}{\delta x} + \frac{\Delta E_{BG}}{\delta x}\right) - \frac{1}{2}\frac{\bar{v_i}}{\bar{m}}\frac{\Delta m}{\delta t}, \tag{4.2}$$

where $\delta x \sim 1\,\mu$m is an estimation of the surface depletion, as well as the distance over which the alloy fraction is varied. In addition, ΔE_{BG} and Δm are the total change of the bandgap and the change of effective mass over the alloy-fraction layer. Using this simplistic approach and using the parameters show in Table 4.1. Since the emission is proportional to the acceleration, in order to present the estimation, all the values obtained where normalized to that of GaAs, and are shown in Fig. 4.4c. The estimation shows qualitative resemblance, and predicts correctly the relative order of the strength of the materials, supporting the qualitative picture that we have presented. Of course,

TABLE 4.1: This table contains the parameters used for the estimation of the emission of all the materials.

Parameter	GaAs	InAs	In>Ga	Ga>In	Unit
$E_{BG}(0)$	1.42	0.35	1.42	0.35	eV
$\bar{m}$	0.066	0.022	0.041	0.041	m_e
ΔE_{BG}	0	0	-1.08	1.08	eV
Δm	0	0	-0.041	0.041	m_e

it is a rather approximate model that does not take into account many subtleties of the carrier dynamics, including the carrier screening of the fields, and the differences in absorption coefficient, among others.

We attribute the enormous difference observed between the annealed and the *as-grown* sample to the defects in the lattice, which will contribute with both scattering centers and traps which will reduce the current transient responsible for the emission. During the annealing process the lattice relaxes and this reduces the number of defects, increasing the mobility and reducing the number of traps, both in the bulk and those on the surface. This is consistent with the analysis of the X-ray diffraction presented earlier. In the case of the inverted gradient, namely Ga>In, the situation is reversed, the band bending caused by the alloy-fraction variation produces an electric field that competes with the surface field, and that points in the direction opposite to the ballistic motion of electrons into the bulk, therefore reducing the emission. The same applies to the $-v\, dm^*/dt$ term, which now points in the opposite direction since the effective mass increases. Finally, we want to point out that both InAs and Ga>In, which are the samples that have Indium at the surface, experience a reduction of the emission with the annealing process. We believe this is because these two samples became semi-metals close to the surface during the baking process, which lead to In segregation that we could observe by optical and atomic-force microscopy images of the annealed samples (not shown). This resulted in a very high carrier density, and therefore high dark conductivity, which in turn reduces the terahertz emission.

4.1.4 Conclusions

In summary, it has been presented a terahertz emission study of $In_xGa_{1-x}As$ gradient samples. It was observed that the emission strongly depends on the direction in which the alloy fraction changes, producing strong emission when the bandgap is narrow in the bulk and larger at the surface and a weak emission in the opposite case. The strong terahertz emission in the first case is comparable to that of InAs. This is explained by the electric

field imposed by the variation of the bandgap energy, which promotes acceleration of electrons towards the bulk in the In>Ga sample, but inhibits the acceleration in the Ga>In case.

Chapter 5

Conclusions

In this thesis I presented results related to the interaction of radiation with semiconductors. To begin with, I presented theoretical simulations of the effect of high-field terahertz pulses on n-doped semiconductors, which resulted in nonlinear optical properties that emerged from inter-valley scattering experienced by strongly accelerated electrons in the material. Secondly, I presented the generation of terahertz pulses from metamorphic InGaAs layers after ultrafast photoexcitation. In the following paragraphs I summarize these two results, provide a general conclusion, and depict some of the potential future work in these two directions.

5.1 Conclusions and discussion

The nonlinear behaviour of carrier dynamics in n-doped semiconductors was discussed in chapter 3. To address the problem, we performed three sets of simulations to emulate a Z-scan experiment for three different THz pulse widths: 0.1, 0.5 and 1.0 ps. The simulation allowed us to track thoroughly the evolution of the inter-valley scatting rates and the population of the valleys. The peak of the inter-valley scattering was located in the vicinity of the peak of the incident terahertz pulse. It was possible to see that for pulses with low field amplitudes the populations only change slowly and the majority of the carriers remain in the Γ-valley, whereas large amplitudes produce fast electron transfer to the L-valley. This change produces variations in the waveforms as well as their spectra which are both amplitude and duration dependent.

The analysis of the transmitted pulses makes possible to see a threshold field, which is different for each pulse duration where the transmitted amplitude shows a change in transmission. Qualitatively, the different thresholds observed for the different incident

pulse duration are due to the fact that the longer pulses accelerate the carriers for longer times, which makes them to gain enough energy to scatter to the L-valley with even lower incident amplitudes.

In conclusion, the Monte Carlo approach allow to analyze thoroughly the evolution of the scattering events and valley populations while an InGaAs sample interacts with a THz pulse. Besides that, it is possible to calculate the time-dependent conductivity to further obtain the transmitted THz pulse, which in turn results in non-linear optical effects experienced by the terahertz pulse itself. In chapter 4, the work regarding the characterization of a heterostructure aimed at the development of new terahertz radiation sources was discussed. There, I presented two different gradient InAs/GaAs heterostructures grown by molecular beam epitaxy. The grown procedure was performed in such a way that while the growing process was carried out, the InAs/GaAs fraction was changed monotonically generating a gradient along the structure. After that, the samples were cleaved into two pieces to preserve one half *as-grown* and to annealed the remaining halves.

After the annealing, the samples were placed into a THz free-space system to generate THz radiation from them. The experiment showed that the emission of *as-grown* InAs is about 13 times the power emitted by the *as-grown* GaAs, while the power emmited by the annealed In>Ga is about 10 times that of *as-grown* GaAs. These observations allowed us to conclude that In>Ga is a forceful emitter almost comparable to annealed InAs, and it is due to its composition: GaAs on the surface (broad band-gap) and, because of the alloy variation, the band-gap narrows down as we move into the bulk producing a strong acceleration of the electrons which is added to the acceleration due to the surface field. The enormous difference between annealed an the *as-grown* is due to defects in the lattice, which contribute with scattering centers and traps that reduce the current transient responsible for the emission.

With this work, it was shown that terahertz emission is strongly dependent on the direction in which the sample is grown, which is the direction in which the alloy fraction varies. This produces strong emission because narrows the band-gap as the carriers go deep into the bulk.

5.2 Further work

For future work, I would like to perform additional experiments with gradient samples in which the thickness of the metamorphic layer can change as well as finding ideal

annealing conditions. Of course, this will involve an enormous effort from the growers and a considerable budget, so this could happen in the coming years.

As for the interaction between terahertz pulses and n-doped InGaAs, I think that additional simulations are desirable, which might include other III-V semiconductors such as InP and GaAs. Then, a thorough comparison with experiments might lead to a better understanding of the details of non-linear interaction between high-field THz pulses and semiconductors.

Bibliography

[1] S. Perlmutter, C. R. Pennypacker, G. Goldhaber, A. Goobar, R. A. Muller, H. J. M. Newberg, J. Desai, A. G. Kim, M. Y. Kim, I. A. Small, et al., Astrophysical Journal Letters **440**, L41 (1995), astro-ph/9505023.

[2] A. G. Riess, A. V. Filippenko, P. Challis, A. Clocchiatti, A. Diercks, P. M. Garnavich, R. L. Gilliland, C. J. Hogan, S. Jha, R. P. Kirshner, et al., The Astronomical Journal **116**, 1009 (1998), astro-ph/9805201.

[3] P. W. Higgs, Phys. Rev. Lett. **13**, 508 (1964), URL https://link.aps.org/doi/10.1103/PhysRevLett.13.508.

[4] F. Englert and R. Brout, Phys. Rev, Lett. **13**, 321 (1964).

[5] K. S. Novoselov, A. K. Geim, S. V. Morozov, D. Jiang, Y. Zhang, S. V. Dubonos, I. V. Grigorieva, and A. A. Firsov, Science **306**, 666 (2004), ISSN 0036-8075, https://science.sciencemag.org/content/306/5696/666.full.pdf, URL https://science.sciencemag.org/content/306/5696/666.

[6] J. M. Kosterlitz and D. J. Thouless, Journal of Physics C: Solid State Physics **5**, L124 (1972), URL https://doi.org/10.1088/0022-3719/5/11/002.

[7] J. M. Kosterlitz and D. J. Thouless, Journal of Physics C: Solid State Physics **6**, 1181 (1973), URL https://doi.org/10.1088/0022-3719/6/7/010.

[8] A. Ashkin and J. M. Dziedzic, Berichte der Bunsengesellschaft für physikalische Chemie **93**, 254 (1989), https://onlinelibrary.wiley.com/doi/pdf/10.1002/bbpc.19890930308, URL https://onlinelibrary.wiley.com/doi/abs/10.1002/bbpc.19890930308.

[9] D. Strickland and G. Mourou, Optics Communications **56**, 219 (1985), ISSN 0030-4018, URL https://www.sciencedirect.com/science/article/pii/0030401885901208.

[10] B. P. Abbott, R. Abbott, T. D. Abbott, M. R. Abernathy, F. Acernese, K. Ackley, C. Adams, T. Adams, P. Addesso, R. X. Adhikari, et al. (LIGO Scientific Collaboration and Virgo Collaboration), Phys. Rev. Lett. **116**, 241103 (2016), URL https://link.aps.org/doi/10.1103/PhysRevLett.116.241103.

[11] J. J. Carty, Science **44**, 511 (1916), ISSN 0036-8075, https://science.sciencemag.org/content/44/1137/511.full.pdf, URL https://science.sciencemag.org/content/44/1137/511.

[12] Y. Gingras, Physics in Perspective **12**, 248 (2010).

[13] J. D. Martin, Physics Today **72**, 30 (2019).

[14] S. Sze and K. Ng, *PHYSICS OF SEMICONDUCTOR DEVICES, 3RD ED* (Wiley India Pvt. Limited, 2008), ISBN 9788126517022, URL https://books.google.com.mx/books?id=6HfSqvSwwMAC.

[15] *Edholm's law of bandwidth - ieee spectrum*, https://spectrum.ieee.org/telecom/wireless/edholms-law-of-bandwidth, [(Accessed on 06/25/2021)].

[16] *Cisco annual internet report - cisco annual internet report (2018–2023) white paper - cisco*, https://www.cisco.com/c/en/us/solutions/collateral/executive-perspectives/annual-internet-report/white-paper-c11-741490.html, [(Accessed on 06/25/2021)].

[17] H. Shams and S. Alwyn, *Photonics, fiber and thz wireless communication* (2017), [(Accessed on 06/25/2021)].

[18] T. Nagatsuma, S. Horiguchi, Y. Minamikata, Y. Yoshimizu, S. Hisatake, S. Kuwano, N. Yoshimoto, J. Terada, and H. Takahashi, Opt. Express **21**, 23736 (2013).

[19] A. J. Seeds, H. Shams, M. J. Fice, and C. C. Renaud, J. Lightwave Technol. **33**, 579 (2015).

[20] Y.-S. Lee, *Principles of Terahertz Science and Technology* (Springer Publishing Company, Incorporated, 2008), 1st ed.

[21] Y. Zhang, C. Wang, B. Huai, S. Wang, Y. Zhang, D. Wang, L. Rong, and Y. Zheng, Applied Sciences **11** (2021), URL https://www.mdpi.com/2076-3417/11/1/71.

[22] P. Kaurav, S. K. Koul, and A. Basu, IEEE Sensors Journal pp. 1–1 (2021).

[23] Z. Vafapour, W. Troy, and A. Rashidi, IEEE Sensors Journal pp. 1–1 (2021).

[24] C. B. Reid, E. Pickwell-MacPherson, J. G. Laufer, A. P. Gibson, J. C. Hebden, and V. P. Wallace, Physics in Medicine and Biology **55**, 4825 (2010), URL `https://doi.org/10.1088/0031-9155/55/16/013`.

[25] Z. Tang, J. Miao, Q. Liu, W. Qu, L. Luo, L. Shang, and H. Deng, Microchemical Journal **169**, 106635 (2021), ISSN 0026-265X, URL `https://www.sciencedirect.com/science/article/pii/S0026265X21007219`.

[26] H. Feng, D. An, H. Tu, W. Bu, W. Wang, Y. Zhang, H. Zhang, X. Meng, W. Wei, B. Gao, et al., Applied Physics B **126**, 1 (2020).

[27] D. Molter, D. Hübsch, T. Sprenger, K. Hens, K. Nalpantidis, F. Platte, G. Torosyan, R. Beigang, J. Jonuscheit, G. v. Freymann, et al., Applied Sciences **11**, 950 (2021).

[28] M. Ibrahim, D. Headland, W. Withayachumnankul, and C. Wang, Journal of Nondestructive Evaluation **40**, 1 (2021).

[29] F. Ellrich, M. Bauer, N. Schreiner, A. Keil, T. Pfeiffer, J. Klier, S. Weber, J. Jonuscheit, F. Friederich, and D. Molter, Journal of Infrared, Millimeter, and Terahertz Waves **41**, 470 (2020).

[30] Y. H. Tao, A. J. Fitzgerald, and V. P. Wallace, Sensors **20**, 712 (2020).

[31] K. Krügener, S. F. Busch, A. Soltani, E. Castro-Camus, M. Koch, and W. Viöl, Journal of Infrared, Millimeter, and Terahertz Waves **38**, 495 (2017).

[32] A. M. Gomez-Sepulveda, A. Hernandez-Serrano, R. Radpour, C. Koch-Dandolo, S. Rojas-Landeros, L. Ascencio-Rojas, A. Zarate, G. Hernandez, R. Gonzalez-Tirado, M. Insaurralde-Caballero, et al., Journal of Infrared, Millimeter and Terahertz Waves **38**, 403 (2017).

[33] C. K. Dandolo, A. Gomez-Sepulveda, A. Hernandez-Serrano, and E. Castro-Camus, Journal of Infrared, Millimeter, and Terahertz Waves **38**, 1278 (2017).

[34] A. K. Singh, A. V. Pérez-López, J. Simpson, and E. Castro-Camus, Scientific reports **10**, 1 (2020).

[35] E. Castro-Camus, M. Palomar, and A. Covarrubias, Scientific reports **3**, 1 (2013).

[36] D. H. Auston, Applied Physics Letters **26**, 101 (1975).

[37] D. H. Auston and K. Cheung, JOSA B **2**, 606 (1985).

[38] K. Humphreys, J. Loughran, M. Gradziel, W. Lanigan, T. Ward, J. Murphy, and C. O'Sullivan, in *The 26th Annual International Conference of the IEEE Engineering in Medicine and Biology Society* (2004), vol. 1, pp. 1302–1305.

[39] W. R. Tribe, D. A. Newnham, P. F. Taday, and M. C. Kemp, in *Terahertz and Gigahertz Electronics and Photonics III* (International Society for Optics and Photonics, 2004), vol. 5354, pp. 168–176.

[40] T. Yasui, T. Yasuda, K.-i. Sawanaka, and T. Araki, Applied Optics **44**, 6849 (2005).

[41] P. U. Jepsen, D. G. Cooke, and M. Koch, Laser & Photonics Reviews **5**, 124 (2011).

[42] E. Dadrasnia, H. Lamela, M. Kuppam, F. Garet, and J.-L. Coutaz, Advances in Condensed Matter Physics **2014** (2014).

[43] C. Caglayan, G. C. Trichopoulos, and K. Sertel, IEEE Transactions on Microwave Theory and Techniques **62**, 2791 (2014).

[44] Z. Song, Z. Wang, and M. Wei, Materials Letters **234**, 138 (2019).

[45] R. Ulbricht, E. Hendry, J. Shan, T. F. Heinz, and M. Bonn, Reviews of Modern Physics **83**, 543 (2011).

[46] C.-S. Yang, C.-M. Chang, P.-H. Chen, P. Yu, and C.-L. Pan, Optics express **21**, 16670 (2013).

[47] T. Kampfrath, K. Tanaka, and K. A. Nelson, Nature Photonics **7**, 680 (2013).

[48] E. Castro-Camus, *Polarisation resolved terahertz time domain spectroscopy* (2006).

[49] R. W. Boyd, *Nonlinear Optics*, Nonlinear Optics Series (Elsevier Science, 2008).

[50] I. Wilke and S. Suranjana, *Nonlinear Optical Techniques for Terahertz Pulse Generation and Detection—Optical Rectification and Electrooptic Sampling*, Optical Science and Engineering (CRC Press, 2007).

[51] J. A. Valdmanis, G. Mourou, and C. W. Gabel, Applied Physics Letters **41**, 211 (1982).

[52] C. O'Sullivan and J. Murphy, *Field Guide to Terahertz Sources, Detectors, and Optics*, Field Guide Series (Society of Photo Optical, 2012), ISBN 9780819491671.

[53] A. H. Chin, J. M. Bakker, and J. Kono, Phys. Rev. Lett. **85**, 3293 (2000).

[54] A. Srivastava, R. Srivastava, J. Wang, and J. Kono, Phys. Rev. Lett. **93**, 157401 (2004).

[55] S. G. Carter, V. Birkedal, C. S. Wang, L. A. Coldren, A. V. Maslov, D. S. Citrin, and M. S. Sherwin, Science (80-.). **310**, 651 (2005).

[56] C. Lange, T. Maag, M. Hohenleutner, S. Baierl, O. Schubert, E. R. Edwards, D. Bougeard, G. Woltersdorf, R. Huber, H. Wen, et al., Phys. Rev. Lett. **78**, 227401 (2008).

[57] T. Kampfrath, K. Tanaka, and K. A. Nelson, Nat. Photonics **7**, 680 (2013).

[58] F. Blanchard, L. Razzari, H. Bandulet, G. Sharma, R. Morandotti, J. C. Kieffer, T. Ozaki, M. Reid, H. F. Tiedje, H. K. Haugen, et al., Opt. Express **15**, 13212 (2007).

[59] J. Hebling, M. C. Hoffmann, H. Y. Hwang, K. L. Yeh, and K. A. Nelson, Phys. Rev. B - Condens. Matter Mater. Phys. **81** (2010).

[60] L. Razzari, F. H. Su, G. Sharma, F. Blanchard, A. Ayesheshim, H. C. Bandulet, R. Morandotti, J. C. Kieffer, T. Ozaki, M. Reid, et al., Phys. Rev. B - Condens. Matter Mater. Phys. **79**, 3 (2009).

[61] F. H. Su, F. Blanchard, G. Sharma, L. Razzari, A. Ayesheshim, T. L. Cocker, L. V. Titova, T. Ozaki, J.-C. Kieffer, R. Morandotti, et al., Opt. Express **17**, 9620 (2009).

[62] M. C. Hoffmann and D. Turchinovich, Appl. Phys. Lett. **96**, 151110 (2010).

[63] F. Blanchard, D. Golde, F. H. Su, L. Razzari, G. Sharma, R. Morandotti, T. Ozaki, M. Reid, M. Kira, S. W. Koch, et al., Phys. Rev. Lett. **107**, 107401 (2011), ISSN 00319007.

[64] W. Kuehn, P. Gaal, K. Reimann, M. Woerner, T. Elsaesser, and R. Hey, Phys. Rev. B - Condens. Matter Mater. Phys. **82**, 075204 (2010).

[65] M. C. Hoffmann, J. Hebling, H. Y. Hwang, K. L. Yeh, and K. A. Nelson, Phys. Rev. B - Condens. Matter Mater. Phys. **79** (2009).

[66] D. Turchinovich, J. M. Hvam, and M. C. Hoffmann, Phys. Rev. B - Condens. Matter Mater. Phys. **85**, 201304 (2012).

[67] C. Lange, T. Maag, M. Hohenleutner, S. Baierl, O. Schubert, E. R. Edwards, D. Bougeard, G. Woltersdorf, and R. Huber, Phys. Rev. Lett. **113**, 227401 (2014).

[68] M. C. Hoffmann, B. S. Monozon, D. Livshits, E. U. Rafailov, and D. Turchinovich, Appl. Phys. Lett. **97**, 231108 (2010).

[69] X. Chai, X. Ropagnol, S. M. Raeis-Zadeh, M. Reid, S. Safavi-Naeini, and T. Ozaki, Phys. Rev. Lett. **121** (2018).

[70] M. Sheik-Bahae, A. A. Said, T. H. Wei, D. J. Hagan, and E. W. Van Stryland, IEEE J. Quantum Electron. **26**, 760 (1990).

[71] J. Lloyd-Hughes, E. Castro-Camus, and M. B. Johnston, Solid State Commun. **136**, 595 (2005), ISSN 00381098, 0507252.

[72] M. B. Johnston, D. M. Whittaker, A. Corchia, A. G. Davies, and E. H. Linfield, Phys. Rev. B **65**, 165301 (2002).

[73] S. C. Corzo-Garcia, M. Alfaro, and E. Castro-Camus, J. Infrared, Millimeter, Terahertz Waves **35**, 987 (2014).

[74] G. R. Fowles, *Introduction to Modern Optics*, Dover Books on Physics (Dover Publications, 2012).

[75] K. Kuznetsov, A. Klochkov, A. Leontyev, E. Klimov, S. Pushkarev, G. Galiev, and G. Kitaeva, Electronics **9**, 495 (2020).

[76] V. Palenskis, L. Minkevičius, J. Matukas, D. Jokubauskis, S. Pralgauskaitė, D. Seliuta, B. Čechavičius, R. Butkutė, and G. Valušis, Sensors **18**, 3760 (2018).

[77] S. G. Muttlak, O. S. Abdulwahid, J. Sexton, M. J. Kelly, and M. Missous, IEEE Journal of the Electron Devices Society **6**, 254 (2018).

[78] D. Ponomarev, A. Gorodetsky, A. Yachmenev, S. Pushkarev, R. Khabibullin, M. Grekhov, K. Zaytsev, D. Khusyainov, A. Buryakov, and E. Mishina, Journal of Applied Physics **125**, 151605 (2019).

[79] T. Hosotani, A. Satou, and T. Otsuji, Applied Physics Express **14**, 051001 (2021).

[80] A. Wudu, D. Rozban, and A. Abramovich, Electronics **9**, 1182 (2020).

[81] T. Sasaki, A. G. Norman, M. J. Romero, M. M. Al-Jassim, M. Takahasi, N. Kojima, Y. Ohshita, and M. Yamaguchi, physica status solidi (c) **10**, 1640 (2013).

[82] M. K. Hudait, Y. Lin, and S. Ringel, Journal of Applied Physics **105**, 061643 (2009).

[83] A. Gocalinska, M. Manganaro, E. Pelucchi, and D. Vvedensky, Physical Review B **86**, 165307 (2012).

[84] Y. Song, T. Kujofsa, and J. E. Ayers, Journal of Electronic Materials **47**, 3474 (2018).

[85] B. Lee, J. Baek, J. Lee, S. Choi, S. Jung, W. Han, and E. Lee, Applied physics letters **68**, 2973 (1996).

[86] M. Choi, I.-Y. Jung, S. Song, and C. S. Kim, Materials Science in Semiconductor Processing **120**, 105251 (2020).

[87] M. Alfaro-Gomez and E. Castro-Camus, Applied Physics Letters **110**, 042101 (2017).

[88] P. Suo, W. Xia, W. Zhang, X. Zhu, J. Fu, X. Lin, Z. Jin, W. Liu, Y. Guo, and G. Ma, Laser & Photonics Reviews **14**, 2000025 (2020).

[89] V. L. Malevich, R. Adomavičius, and A. Krotkus, Comptes Rendus Physique **9**, 130 (2008), recent developments in terahertz optoelectronics.

[90] M. Reid and R. Fedosejevs, Applied Physics Letters **86**, 011906 (2005).

[91] R. Ascázubi, C. Shneider, I. Wilke, R. Pino, and P. S. Dutta, Phys. Rev. B **72**, 045328 (2005).

[92] R. Ascázubi, I. Wilke, K. Denniston, H. Lu, and W. J. Schaff, Applied Physics Letters **84**, 4810 (2004).

[93] J. N. Heyman, N. Coates, A. Reinhardt, and G. Strasser, Applied Physics Letters **83**, 5476 (2003).

[94] M. F. S. Ferreira, E. Castro-Camus, D. J. Ottaway, J. M. López-Higuera, X. Feng, W. Jin, Y. Jeong, N. Picqué, L. Tong, B. M. Reinhard, et al., Journal of Optics **19**, 083001 (2017).

[95] R. A. Lewis, Journal of Physics D: Applied Physics **47**, 374001 (2014).

[96] J. Lloyd-Hughes, E. Castro-Camus, M. D. Fraser, C. Jagadish, and M. B. Johnston, Phys. Rev. B **70**, 235330 (2004).

[97] M. B. Johnston, D. M. Whittaker, A. Corchia, A. G. Davies, and E. H. Linfield, Phys. Rev. B **65**, 165301 (2002).

[98] J. Lloyd-Hughes, E. Castro-Camus, and M. Johnston, Solid State Communications **136**, 595 (2005), ISSN 0038-1098.

[99] P. Bone, J. Ripalda, G. Bell, and T. Jones, Surface Science **600**, 973 (2006).

[100] G. H. Kim, J. B. Choi, J. I. Lee, S.-K. Kang, S. I. Ban, J. S. Kim, J. S. Kim, S. H. Lee, and J.-Y. Leem, MRS Online Proceedings Library Archive **696** (2001).

[101] D. Benyahia, K. Michalczewski, A. Kębłowski, P. Martyniuk, J. Piotrowski, A. Rogalski, et al., Optical and Quantum Electronics **48**, 1 (2016).